From ground motion simulations to landslide occurrence prediction

Ashok Dahal[1*], David Alejandro Castro Cruz[2], Hakan Tanyas[1], Islam Fadel[1], Paul Martin Mai[2], Mark van der Meijde[1], Cees van Westen[1], Raphaël Huser[3], Luigi Lombardo[1]

Abstract

Ground motion simulations solve wave equations in space and time, thus producing detailed estimates of the shaking time series. This is essentially uncharted territory for geomorphologists, for we have yet to understand which ground motion (synthetic or not) parameter, or combination of parameters, is more suitable to explain the coseismic landslide distribution. To address this gap, we developed a method to select the best ground motion simulation using a combination of Synthetic Aperture Radar Interferometry (InSAR) and strong motion data. Upon selecting the best simulation, we further developed a method to extract a suite of intensity parameters, which we used to both bivariately and multivariately analyse coseismic landslide occurrences taking the Gorkha earthquake as a reference. Our results show that beyond the virtually unanimous use of peak ground acceleration, velocity, or displacement in the literature, different shaking parameters could play a more relevant role in landslide occurence. These parameters are not necessarily linked to the peak values but mostly linked to the actual displacement, velocity, frequency content and shaking duration, elements too often neglected in geomorphological analyses. This in turn implies that we have yet to fully acknowledge the complexity of the interactions between full waveforms and hillslope responses.

Keywords: Landslide Modeling; Earthquake simulation; Geophysics; Geotatistics; InSAR.

[1]University of Twente, Faculty of Geo-Information Science and Earth Observation (ITC), PO Box 217, Enschede, AE 7500, Netherlands

[2]Physical Sciences and Engineering (PSE) Division, King Abdullah University of Science and Technology (KAUST), Thuwal, Saudi Arabia

[3]Computer, Electrical and Mathematical Sciences and Engineering (CEMSE) Division, King Abdullah University of Science and Technology (KAUST), Thuwal, Saudi Arabia

1 Introduction

Coseismic landslides are a cascading hazard caused by earthquake ground motion and constitute a threat to infrastructure and communities in tectonically-active mountainous regions (Fan et al., 2019). This is the case because landslides have the dual ability to cause financial and life losses associated with short (Nowicki Jessee et al., 2020) and long-term consequences (Oven et al., 2021) and also to do the same by hindering the timely arrival of rescue teams during the emergency phases (Williams et al., 2018). Therefore, the prediction of areas likely affected by co-seismic landslides could play a role of prime importance in terms of emergency response (e.g. Robinson et al., 2017) and long-term planning actions (e.g. Lombardo and Tanyas, 2021). In this context, the footprint of ground shaking needs to be accurately assessed to better predict the spatial distribution of co-seismic landslides.

The increasing number of publicly available landslide inventories (e.g. Schmitt et al., 2017; Tanyaş et al., 2019) has resulted in an increasing number of coseismic landslide hazard models with respect to ground motion. However, this type of studies hardly make use of modern ground motion simulation techniques (e.g., Guatteri et al., 2004; Peter et al., 2011).

This research explores the use of synthetic ground motion obtained via full waveform simulations in the context of landslide modelling. To do so, we develop a procedure to recognise the best parameterisation for earthquake simulations representative of the Gorkha earthquake that occurred on 24^{th} April 2015. The simulations are generated via the Salvus software (Afanasiev et al., 2018). On the basis of the synthetic ground motion, we then carry out bivariate and multivariate analyses to correlate the coseismic landslide distribution to a large suite of ground motion parameters. From these, we isolate the ones that explain the slope failures the most. Overall, we hypothesise that the full spectral information contained in the waveforms can be used to better understand the genesis of coseismic landslides.

2 Background

Spatial distribution of co-seismic landslides is controlled by variations in the terrain, soil and ground motion characteristics (Fan et al., 2019). Terrain and soil characteristics essentially stay the same at the scale of human perception and therefore their influence on landslide activation is mainly interpreted in a predisposing manner (Donati and Turrini, 2002). As for the ground motion, its spatial and temporal dynamics constitute the main trigger of a single or of a population of coseismic slope failures (Lee, 2014). For this reason, dedicated analyses on the ground motion are required to understand slope responses (Nowicki et al., 2014). In fact, the ground motion varies not only as a function of depth and magnitude but also thanks to the contributions due to rupture propagation, fault geometry, velocity structure and local site conditions (Oglesby and Mai, 2012; Vyas et al., 2016), which also controls the spatial distribution of co-seismic landslides (Jibson, 2011; Fan et al., 2019).

Traditionally, the geomorphological community has attempted to study the dependence between landslide occurrences and seismic shaking by using two major sources of ground motion parameters: strong-motion databases (SMDs) and ground motion prediction equations (GMPEs). The former are repositories of seismic records collected within networks often operated nationally (e.g., Pacor et al., 2011) or even globally (e.g., Chiou et al., 2008). Time series are recorded at locations where sensors are deployed and spatially-continuous shaking parameters are then obtained through interpolation (e.g., Wald et al., 1999).In terms of the prediction of landslide occurrences, SMDs are primarily used to build the link between ground motion and associated landslide displacements (Jibson, 1993, 2007). This link is expressed by various regression equations in the literature and further exploited to develop predictive displacement models through Newmark (Newmark, 1965) sliding block model (Jibson et al., 2000; Gallen et al., 2017).This is to say that, SMDs are quite valuable data sources shedding light on the genesis of co-seismic slope failures. However, a number of limitations affect the use of these data sources to understand and model coseismic landslides. The major limitation of SMDs is that, even though they can provide accurate observation of ground motion, they lack the required spatial coverage to finely resolve the shaking at the level of single slopes. Specifically, any interpolative procedure acts as a spatial smoother, thus removing precious information for the landslide modelling. This is even more exacerbated in low to medium-income countries where very few strong-motion stations are present. But, even for very dense seismic networks such as the K-Net in Japan (Aoi et al., 2004) or the USArray in the United States (Meltzer et al., 1999), local and spatially-continuous variations in the ground motion signal due to soil and/or topographic amplification are hardly observable. In fact, to provide spatially-continuous variables representing ground motion footprint, SMDs are also used as inputs for GMPEs.

GMPEs refer to data-driven models capable of empirically relating the ground motion signal to earthquake source characteristics, attenuation and distributions of Vs30 data (Atkinson and Boore, 2011). The most common products of such models boil down to a few summary statistics of the original waveform, these being for instance, the Peak Ground Acceleration (PGA) or the Peak Ground Velocity (PGV) (García et al., 2012; Worden and Wald, 2016). This is mainly the case because GMPEs are designed to estimate ground motion parameters, and it is not possible to resolve the full waveform uniquely via statistical relationships because of the complex interaction of the waveform with the medium it interacts with. Also, GMPEs are derived from past events or from different regions, and can suffer from large uncertainties and bias (Castro-Cruz et al., 2021); among which are the limited number of observations on strong motion data they are built upon. As a result, GMPEs can be ill-defined and the ground motion they generally estimate poorly reflects some important characteristics of earthquake waveforms associated with, for instance, topographic amplification, duration of shaking and/or rupture directivity, which plays an important role in landslide occurrence (Fan et al., 2019).

To surpass those limitations, numerical physical models have been implemented to simulate landslides because of the importance of earthquakes in abruptly raising rates of erosion, sediment transport, and deposition (e.g., Simonett, 1967; Pearce and Watson, 1986). Using numerical simulations, several works (e.g., Bouchon, 1985; Geli et al., 1988; Tripe et al., 2013) found the high relevance of the site effects of a slope on the amplification of the ground motion. Following this, many works also saw how the 3d effects from geology and topography are relevant in landslide occurrence by studying the incoming waves (e.g., Khalil and Lopez-Caballero, 2021; He et al., 2020; Dunham et al., 2022). Because those analyses are at local scales, they implement complex constitutive models for the soil materials' resistance and rupture. This paper aims to perform simulation at a large scale. In such models are not possible to follow complex constitutive laws, first because of the need for more specific information on all the area and the computational cost. It is still challenging to join regional physic earthquake simulation with a landslide analysis. Huang et al. (2020) employ a SEM simulation to recreate the ground motion and use this at each part of the region a Newark analysis to study the landslide occurrences. In this paper, we also use SEM simulations to recreate the earthquake but try to analyze the landslide through a statistic analysis.

Even with such limitations, virtually every single coseismic landslide study so far adopts GMPE-based estimates of ground motion, mostly because of their accessibility as part of the USGS ShakeMap service (Wald et al., 2008). ShakeMap system provides near-real-time estimates of ground motion parameters globally for any significant earthquake (Mw¿5.5). These estimates are updated over time with new data acquisitions, which is mostly the case for large earthquakes such as the 2015 Gorkha event. Specifically, GMPEs allocated to derive ground motion estimates depending on earthquake mechanism and seismotectonic setting, rupturing geometry, citizen science feedback regarding shaking intensity and SMDs are used to update ShakeMap products over time (Wald et al., 2022). The most widely used parameters in landslide studies are the PGA, PGV, and Modified Mercalli Intensity (MMI) (e.g., Nowicki et al., 2014; Lombardo et al., 2018; Nowicki Jessee et al., 2018). However, looking beyond the typical reach of the landslide community, geophysicists are used to representing the full waveform via a much larger range of ground motion parameters, each one carrying its own specific physical meaning (see Riddell, 2007; Shahaki and Celikag, 2019). These parameters can be either computed individually or as multiple respective combinations, and their strength resides in the ability to carry much richer shaking information as compared to the few ones mentioned above.

Beyond the SMD and GMPE options largely explored by the geomorphological community, a third possibility is routinely explored by seismologists since 1960'ies, in the form of physics-based simulations (e.g., Harris et al., 2011; Imperatori and Mai, 2013). An extensive description of these methods and their formulation is provided in part II of the book authored by Igel (2017). Among these, the most accurate methods include finite difference method (Alterman and Karal Jr, 1968), finite element method (Lysmer and Drake, 1972), and spectral element method (Seriani and Priolo, 1994; Faccioli et al., 1996). They essentially solve for the ground motion (mostly velocity or displacement) in space and time using wave elastic equations. Specifically, their use is particularly suited for large-scale wavefield reconstructions, obtained by solving wave equations according to specific source mechanisms in a 3D space partitioned according to a mesh, whose structure mimics the earth's sub-surface and topography. These simulations are computationally expensive, and the input parameters often contain large uncertainties. The major sources of uncertainties are the source model, which largely depends on the inversion mechanism and input data; velocity structure which depends on the location; and the model parameters, which need to be carefully selected to obtain a good fit. In data-poor regions where strong motion records are limited, selecting the best combination of the finite fault model, velocity structure, and the model parameter is difficult because of a limited number of observations to compare the full waveform solutions against.

Given these constraints, there are only a few studies aiming to exploit 3D earthquake simulations to better assess the occurrence of co-seismic landslides. Those studies either couple the spectral element method with the Newmark sliding block analysis (Huang et al., 2020; Chen and Wang, 2022; Sun and Huang, 2023) or the material point method (Feng et al., 2022) to accurately identify landslide displacements, or examine the spatial distribution of co-seismic landslides with respect to peak modeled ground motions (Harp et al., 2014; Dunham et al., 2022). Among these studies, the research carried out for the 2015 Gorkha earthquake (Dunham et al., 2022) is particularly important because this was the first time that topographically amplified seismic velocity and acceleration and their relation to landslide sizes were investigated for such a large area ($1^\circ \times 2^\circ$) and a large earthquake-induced landslide event ($\approx$ 25,000 co-seismic landslides) using a 3D earthquake simulation.

In this broad overview of the current state of the coseismic landslide literature, the choice of the most suitable ground motion parameter to explain the landslide scenario have been rarely discussed in detail. As a result, this research gap hinders the development of a holistic understanding of the ground motion and slope interactions.

3 Material

3.1 Study area

The experiments part of this research have been run in the area affected by the 2015 Gorkha (Nepal) earthquake of magnitude Mw7.8 that occurred on 24^{th} April 2015. This was one of the largest the largest ever recorded earthquake across the whole Main Himalayan Thrust (MHT). The earthquake is the result of the dominant thrust faulting mechanism typical of the MHT; the strike and dip angle of the seismogenic fault is estimated to be 293° and 7°, respectively (Ekström et al., 2012). Zhang et al. (2016) estimate that the rupture propagation of the mainshock nucleated near the hypocenter and propagated along the dip direction southeastwards with a total duration of 70 seconds and maximum slip of 5.2 meters.

3.2 Landslide inventory

Aside from the infrastructural damage, approximately 25,000 landslides were triggered by the 25 April 2015 Mw7.8 Gorkha earthquake and its aftershocks (Roback et al., 2018). The authors mapped co-seismic landslides triggered by the mainshock using multi-sensor high-resolution optical images (0.2-0.5 meters). The resulting polygonal landslide inventory discerns source and deposition areas, whose combined extent leads to a landslide area distribution centred at a mean value of 3,473 m^2, with a standard deviation of 11,240 m^2. The largest one, Langtang Valley Landslide, reached up to 1,720,500 m^2.

Being the focus of this work aimed at explaining coseismic landslide occurrences according to a suite of synthetic ground motion parameters, the Gorkha earthquake certainly satisfies the requirements of landslide inventory quality and completeness (Tanyaş and Lombardo, 2020). As for the requirements for the simulations, further details will be provided in Section 4.

3.3 Observations and spatial domain

Figure 1, shows the mainshock-induced landslide inventory (red polygons), together with the approximate rupture plane (yellow rectangle), ground motion simulation domain (grey rectangle) and the actual test site (green shaded area). Notably, the simulation domain extends over an area of $4° \times 3°$. The asymmetry in the two directions is due to the main thrust whose expression was mainly along the eastward direction.

To compare our earthquake simulations against ground motion records, we accessed the data collected at one seismic station (labelled as KATNP in Figure 1) as well as six high-frequency Global Navigation Satellite Systems (GNSS) stations. The data recorded at KATNP was processed and shared by Shigefuji et al. (2022) whereas the GNSS station data was processed and shared by Galetzka et al. (2015).

As for how to partition the test site into meaningful mapping units, we opted for a slope unit partition (Alvioli et al., 2016). These slope units represent half sub-basins and constitute the building block of our model for the landslide analyses. From the slope unit map, all the areas below the 10° slope were removed to exclude flat areas from our analysis. Details on the slope unit generation are provided in Dahal and Lombardo (2022).

4 Methods

Our analytical protocol involves: *i)* ground motion simulation and *ii)* their validation, *iii)* extraction of ground motion parameters and *iv)* geo-statistical bivariate and multivariate data-driven analyses of landslide occurrence data. Each of these steps required multiple nested operations who's details and justifications will be provided in the following sections.

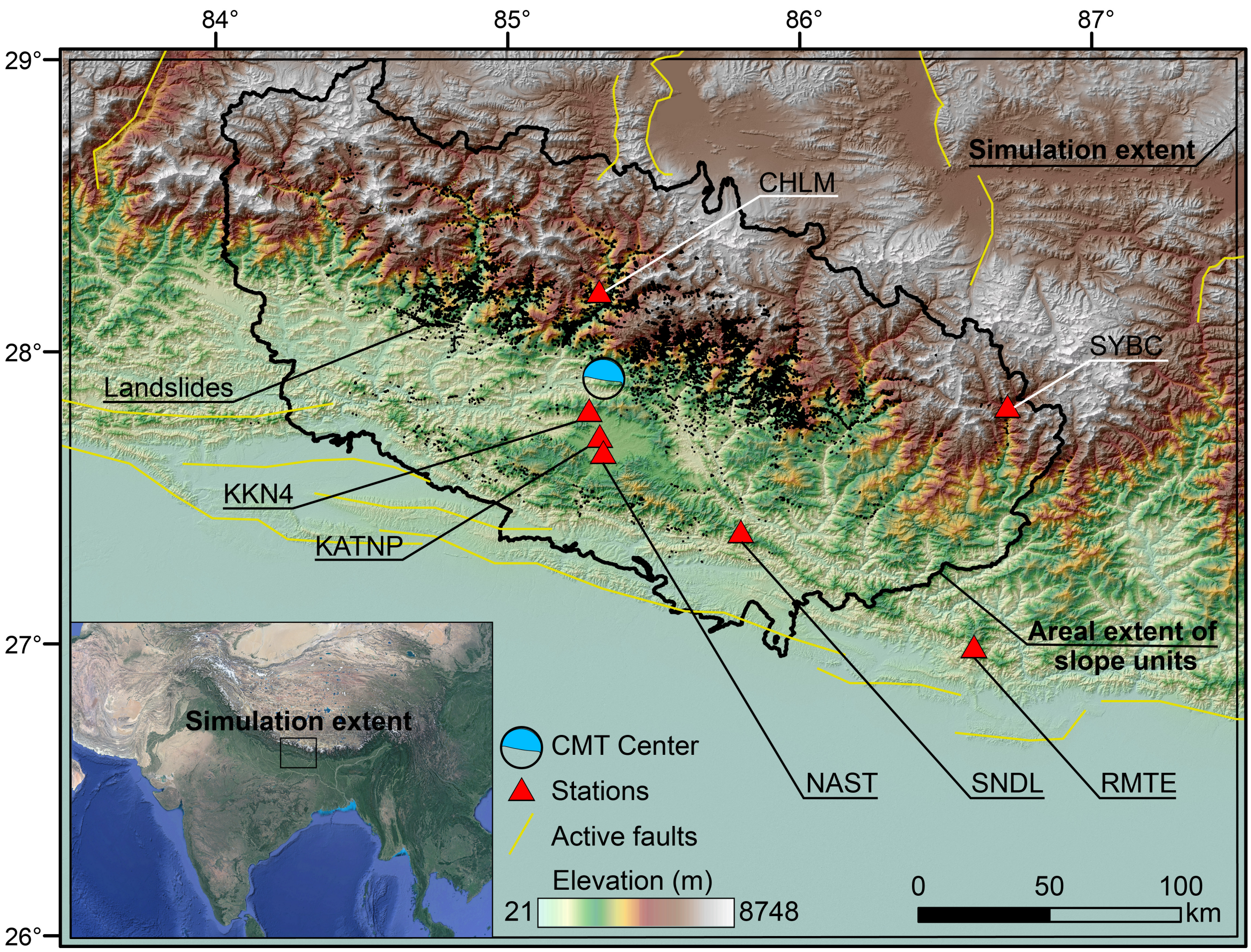

Figure 1: Study area representing the ground motion simulation domain, the test site for landslide analyses partitioned into slope units (indicated by green polygons) and the landslide inventory. The stations in the map represent the ground motion recording stations, and the CMT centre is the centroid of the moment tensor generated by global CMT project. Active faults are also shown characterising the tectonics of the MHT fault zone.

4.1 Simulation configuration

To generate full waveform simulations we used Salvus (Afanasiev et al., 2018). This is a community software which solves for the 3D elastic wave equation using spectral element method. The fundamental requirements for Salvus are: *i)* a source model, *ii)* a simulation mesh, and *iii)* a suite of model hyperparameters; detailed description of each requirement is provided below.

The fault model of the 25 April 2015 Mw7.8 Gorkha earthquake has been extensively studied, each one based on different types of data including, teleseismic, GNSS, InSAR and their combinations. Some of those sources are the point source model derived by both the Global Centroid Moment Tensor (GCMT) project (Ekström et al., 2012) and United States Geological Survey (USGS) (USGS, 2015). There are also four well known finite fault models derived for the same event using multiple combinations of the teleseismic and geodetic data (Hayes et al., 2015; Yagi and Okuwaki, 2015; Kobayashi et al., 2016; Wei et al., 2018). The model from Wei et al. (2018) heavily relied on InSAR data from Sentinel-1 and ALOS PALSAR missions, together with the teleseismic data. Conversely, the models proposed by Hayes et al. (2015) and Yagi and Okuwaki (2015) have not used INSAR data but rather teleseismic and strong motion ones. Moreover, Kobayashi et al. (2016) has used displacement points from InSAR (21 in total), and GNSS stations together with teleseismic data. In this work, we tested both the point source solutions mentioned above and the resulting ground simulations were unsatisfactory compared to those obtained from the full fault models (unreported results). As for the latter, we had to test which of the four faults reproduced the most realistic wavefield.

Notably, Nepal does not have a permanent seismic array deployed with a high spatial resolution. For the specific case of the Gorkha earthquake, most of the available seismic stations were located in the sedimentary basin, where the underlying velocity structure is not known (Kobayashi et al., 2016). Therefore, with only 7 stations available (see Fig. 1), any validation of the forward simulation was difficult. Thus, to create a complementary testing scheme, we integrated InSAR data in our validation protocol (see Section 4.2).

To design the mesh required for the 3D elastic wave propagation we opted to use the waveform adaptive mesh recommended by Thrastarson et al. (2020). The depth of the mesh was set at 35 km below the mean sea level. This choice followed a criterion where enough volume was defined below the deepest point along the finite fault solution to remove any source of reverberation from the bottom. As for the top, the surface topography was added above the mean sea level. A 50-meter topography was obtained from the global multi resolution topography data synthesis project (Ryan et al., 2009). The horizontal distance between the mesh elements was automatically calculated within Salvus, based on the velocity of the S-wave and the design frequency. The resulting mesh spatial resolution was around 300 meters, a resolution capable to resolve frequencies up to 3.0 Hz. However, the four source models considered here were designed with an upper limit of 1.0 Hz which limited the resolved frequency range.)

Once the mesh was created, each element in the mesh was populated with the velocity and density structure. Each of the four source models we considered had different velocity structure in their source model inversion, which we maintained in the respective simulations. Specifically, for the finite fault model of Wei et al. (2018), we used velocity structure from Mahesh et al. (2013). For the remaining source models, we used instead the velocity density structure they respectively assumed during the fault model inversion (Kobayashi et al., 2016; Hayes et al., 2015; Yagi and Okuwaki, 2015). All fault solutions and velocity structure information are available at the SRCMOD database (Mai and Thingbaijam, 2014). With the velocity structure and mesh elements defined, we then calculated the Mass and Stiffness matrices required by the spectral element method before propagating the elastic waves from source model (Igel, 2017).

The total duration of each simulation was set to 200 seconds to accommodate for roughly three times the Gorkha rupture duration (≈60"; Wei et al., 2018). Out of the simulated field, we opted to store the full velocity waveform in time domain. We did so for each mesh element and only at the earth surface. Moreover, we also recorded the full waveform at locations defined by the seven available stations (see Fig. 1). Furthermore, we also added an absorbing boundary 16 km in each direction except the free surface boundary to avoid reflections of the seismic wave. The absorbing boundary width was set on the basis of multiple (unreported) tests, with starting width of 4 km and up to 64 km. All simulations were performed in a HPC environment distributed over 42 CPU cores. The resulting computational time for a single fault solution was $\approx$ 96 hours for a total of $\approx$ 4032 CPU hours.

4.2 Validation of simulation

The most accepted method to validate the ground motion simulation relies on the comparison of synthetic and recorded waveforms. The scarse and non-uniform spatial distribution of the Nepalese stations can be visualized in Figure 1, where four out of the seven stations are clustered near the CMT center (within 35 km), whereas the remaining three are only available in the eastern sector ($\approx$ 100-200 km). Such distribution is not sufficient to support a robust validation of the synthetic waveform simply because we could not compare synthetic waveforms in all directions and distances. Moreover, the number of stations is very low, to begin with. Therefore, we implemented a validation protocol that would include the InSAR displacement together with the standard waveform comparison. This dual information contextually provides an overview of the ground motion on the basis of few locations but where a full time series is available. As for the InSAR component, it trades the breadth of temporal data with space, as for each InSAR point only one displacement value can be obtained. However, this comes with a much larger and continuous spatial coverage.

Notably, a similar approach has been tested by (Paolucci et al., 2015; Shen et al., 2022), although they only use the average ground displacement information pertaining to the last 5 seconds of the simulation. Conversely, we opted for checking the cumulative displacement over the full time-series, without taking the arbitrary choice of a fixed time window. As a result, our validation method goes beyond the visual comparison proposed by Paolucci et al. (2015) ensuring a quantitative assessment.

Specifically, our approach requires information on the total displacement along the Line of Sight (LoS) from the InSAR data. To obtain it, we used pre (22 Feb 2015) and post (3 May 2015) ALOS PALSAR images acquired in ScanSAR mode. The LoS displacement was obtained by using the GMTSAR software (Sandwell et al., 2011) while the phase unwrapping was done through SNAPHU (Chen and Zebker, 2002). For reasons of conciseness, the InSAR protocol is not specified here but we followed the same protocol described in Lindsey et al. (2015). Upon completion of the InSAR step, we calculated the unit vectors pointing towards the position of the satellite at each location on the surface, which is then used to convert the total simulated displacement to the LoS displacement.

Theoretically, one should be able to retrieve the total displacement through InSAR. Similarly, the spectral element method should also be able to model such cumulative displacement in all directions. Therefore, the former could be used to validate the latter.

To obtain the synthetic cumulative displacement, we filtered out frequencies above 1.5 Hz and then calculated the cumulative displacement over the whole time series. As a result, we obtained a measure of cumulative displacement along east-west, north-south and up-down directions, which we further aggregated along the InSAR LoS direction by multiplying with the unit vectors. The resulting spatial pattern can then be correlated to the InSAR displacement using the Pearson's correlation coefficient, as shown in equation 1.

$$r = \frac{\sum_{i=1}^{n}(x_i - \overline{x})(y_i - \overline{y})}{\sqrt{\sum_{i=1}^{n}(x_i - \overline{x})^2}\sqrt{\sum_{i=1}^{n}(y_i - \overline{y})^2}}, \tag{1}$$

where x is the observed LoS displacement from the InSAR observation and $\overline{x}$ is the mean displacement. y and $\overline{y}$ are the simulated LoS displacement and mean simulated LoS displacement, respectively. The Pearson's coefficient r is the correlation coefficient which provides represents the correlation between the variables.

4.3 Ground motion parameter extraction

Upon completion of the ground motion simulations, to understand how synthetic waveform correlate with coseismic landslide scenario – beyond the conventional PGA, PGV, AI, and SA – we computed a suite of ground motion parameters, the list of which is presented in Table 1. Prior to that, the three ground motion components have been aggregated taking their dot product.

4.4 Geostatistical evaluation

For the geostatistical evaluation, we employed several methods to measure the strength of the dependence between ground motion parameters and landslides' distribution. The major methods we employed encompass: cross-correlation (Pearson, 1895), bivariate point biserial

Name	Abbr.	Formula	Source
		Acceleration Related Parameters	
Earthquake Power Index	Pa	$\mathrm{P_a} = \frac{1}{\mathrm{t_2 - t_1}} \int_{\mathrm{t_1}}^{\mathrm{t_2}} \mathrm{a^2(t)dt}$	Housner (1975)
Peak Ground Acceleration	PGA	$\mathrm{A_{max}} = \max \lvert \mathrm{a(t)} \rvert$	Gutenberg and Richter (1942)
Arias Intensity	IA	$\mathrm{I_A}(\xi) = \frac{\cos^{-1}\xi}{\mathrm{g}\sqrt{1-\xi^2}} \int_0^{\mathrm{t_f}} \mathrm{a^2(t)dt}$	Arias (1970)
Squared Acceleration	Asq	$a_{sq} = \int_0^{t_f} a^2(t)dt$	Housner and Jennings (1964)
RMS Power Index	Arms	$\mathrm{a_{rms}} = \sqrt{\mathrm{P_a}}$	Housner and Jennings (1964)
Root Squared Acceleration	Ars	$\mathrm{a_{rs}} = \sqrt{\mathrm{a_{sq}}}$	Housner (1970)
Characteristic Intensity	Ic	$\mathrm{I_C} = \mathrm{a_{rms}^{1.5} t_d^{0.5}}$	Park et al. (1985)
Compound Index	Ia	$I_a = a_{\max} t_d^{1/3}$	Riddell and Garcia (2001)
		Velocity Related Parameters	
Compound Index	If	$\mathrm{I_F} = \mathrm{v_{max} t_d^{0.25}}$	Fajfar et al. (1990)
Compound Index	Iv	$I_v = v_{\max}^{2/3} t_d^{1/3}$	Riddell and Garcia (2001)
Peak Ground Velocity	PGV	$\mathrm{V_{max}} = \max \lvert \mathrm{v(t)} \rvert$	Rosenblueth (1964)
Cumulative Velocity	CUV	$\mathrm{V_{cu}} = \int_{\mathrm{t_0}}^{\mathrm{t}_n} \mathrm{a(t)dt}$	EPRI (1988)
Power Index	Pv	$\mathrm{P_v} = \frac{1}{\mathrm{t_{95} - t_5}} \int_{\mathrm{t_5}}^{\mathrm{t_{95}}} \mathrm{v^2(t)dt}$	Housner (1975)
Squared Velocity	Vsq	$\mathrm{v_{sq}} = \int_{\mathrm{o}}^{\mathrm{t_f}} \mathrm{v^2(t)dt}$	Housner and Jennings (1964)
RMS Power Index	Vrms	$\mathrm{v_{rms}} = \sqrt{\mathrm{P_v}}$	Housner and Jennings (1964)
Root Squared Velocity	Vrs	$\mathrm{v_{rs}} = \sqrt{\mathrm{v_{sq}}}$	Housner (1970)
Potential Destructiveness	Pd	$\mathrm{P_D} = \frac{\mathrm{I_A}}{v_{\mathrm{o}}^2}$	Araya and Saragoni (1980)
Spectral Intensity	SI	$\mathrm{S_I}(\xi) = \int_{0.1}^{2.5} \mathrm{S_v}(\xi, \mathrm{T})\mathrm{dT}$	Housner (1952)
		Displacement Related Parameter	
Peak Ground Displacement	PGD	$\mathrm{D_{max}} = \max \lvert \mathrm{D(t)} \rvert$	Newmark and Hall (1973)
Cumulative Displacement	CUD	$\mathrm{D_{cu}} = \int_{\mathrm{t_0}}^{\mathrm{t}_n} \mathrm{v(t)dt}$	Walsh and Watterson (1987)
Power Index	Pd	$\mathrm{P_d} = \frac{1}{\mathrm{t_{95} - t_5}} \int_{\mathrm{t_5}}^{\mathrm{t_{95}}} \mathrm{d^2(t)dt}$	Housner (1975)
Square Displacement	Dsq	$\mathrm{d_{sq}} = \int_{\mathrm{o}}^{\mathrm{t_f}} \mathrm{d^2(t)dt}$	Housner and Jennings (1964)
RMS Power Index	Prms	$\mathrm{d_{rms}} = \sqrt{\mathrm{P_d}}$	Housner and Jennings (1964)
Root Squared Displacement	Drs	$\mathrm{d_{rs}} = \sqrt{\mathrm{d_{sq}}}$	Housner (1970)
Compound Index	Id	$\mathrm{I_d} = \mathrm{d_{max} t_d^{1/3}}$	Riddell and Garcia (2001)
		Other Parameters	
Significant Duration	Sigdur	$Significant\ duration$	Trifunac and Brady (1975)
Maximum Frequency	MaxFreq	$F_{maximum\ amplitude}$	Millen (2019)
Shaking Intensity Rate	Sir	$SIR = I_{a5-75}/D_{5-75}$	Dashti et al. (2010)
Ratio of PGV and PGA	PGVpA	PGV/PGA	Poreddy et al. (2022)

Table 1: Table representing the list of equations used to extract the ground motion intensity parameters and their sources.

correlation (Gupta, 1960), and local spatial autocorrelation (Ord and Getis, 1995). Furthermore, to understand the combined influence of the ground motion parameters on the landslide occurrence, we performed a variable selection routine as part of a susceptibility model based on a frequentist Binomial Generalized Additive Model (GAM; Hastie, 2017). Ultimately, we measured the deviation in performance calculated between our best susceptibility model and a model built on the basis of GMPEs, accessed through the USGS ShakeMap service. The latter were initially published right after the Gorkha earthquake and refined with time, thus providing three empirical versions of the ground motion (2015, 2017 and 2020; García et al., 2012; USGS, 2015), which we tested one by one. Further details on each of these statistical tests are provided in Appendix A.

5 Results

5.1 Ground motion validation

The comparison between an observed and estimated ground motion for each of the four fault solutions is graphically shown in Figure 2. There, the signal at each of the seven stations is plotted along the three main directions. Among the synthetic signals, we can notice that in most cases amplitudes and frequencies are suitably represented. However, on a few occasions, a marked difference stands out. For instance, KATNP and NAST show a general underestimation along the horizontal directions, likely due to soil amplification in the Kathmandu valley. As for the rest, some mismatch appears in SNDL, but this is confined to timing rather than amplitude. However, the misfits mentioned above are significantly reduced when checking the ground motion generated via the finite fault model proposed by Wei et al. (2018). This has been further verified by evaluating the ground motion simulation via the Kristekova method (Kristeková et al., 2006), which shows that the Wei et al. (2018) fault model produces the best simulation results. A detailed description of the validation and its results for all the fault models is presented in B. To visualize the simulation in the examined spatio-temporal domain, we have plotted a few summary snapshots of the velocity magnitude at different time steps for the best-fitting simulation in Figure 3.

The results of the InSAR analyses are shown in Figure 4. There, similarly to the waveform comparison highlighted before, the best fit corresponds to the simulations made using the fault solution of Wei et al. (2018). In this case though, it is also possible to visually appreciate a ranking of the four available solutions, with the second best being obtained with the fault model from Kobayashi et al. (2016), followed by Yagi and Okuwaki (2015) and Hayes et al. (2015). It is important to note that the worst agreement between cumulative displacements is obtained with a source model that was obtained right after the earthquake occurrence. And yet, the obtained Pearson correlation is still quite acceptable (0.61).

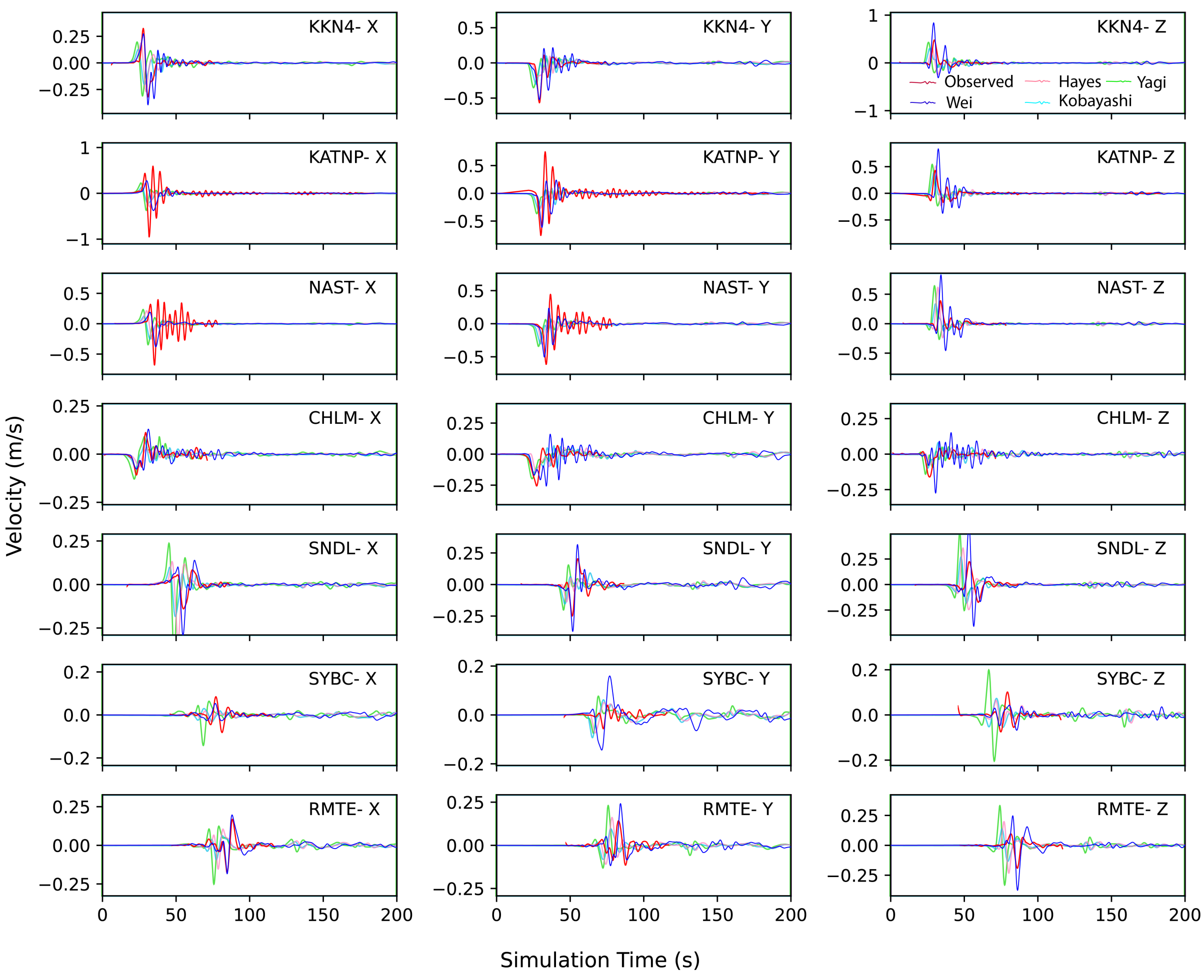

Figure 2: Comparison of simulated and observed waveforms. Best fit corresponding to the simulations generated on the basis of the fault solution proposed by Wei et al. (2018).

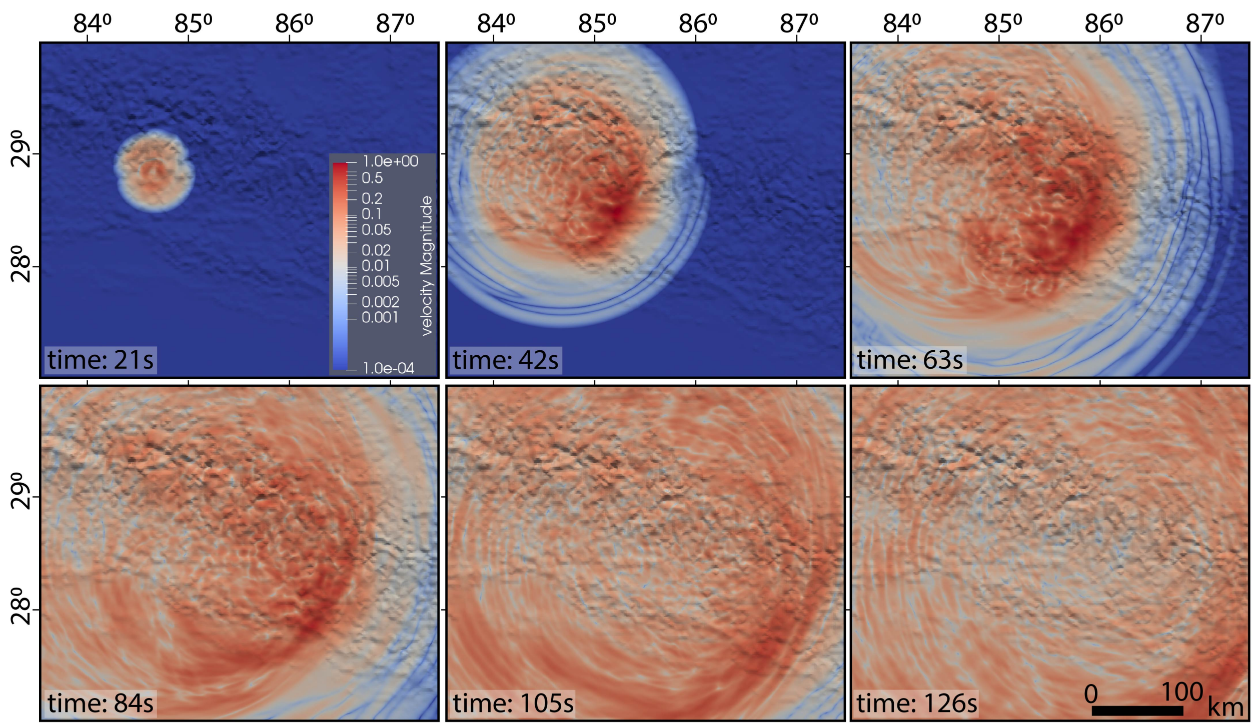

Figure 3: Snapshot of velocity wavefield at different timesetps for the best fitting simulation developed on the basis of fault model proposed by Wei et al. (2018).

5.2 Evaluation of Shaking Parameters for landslide prediction

From the synthetic ground motion records, we extracted the suite of 28 shaking parameters listed in Table 1 with the aim of testing them to predict unstable slopes. For this reason, we included an initial exploratory step where we examined the pairwise correlation among the 28 intensity summaries (see Fig. 5). What stands out is that few of them are dependent on each other.

To explore ground motion effects on landslide occurrences, we opted for a binary (presence/absence) visualization of the parameters distribution at specific slope steepness intervals. This is shown through violin plots (see Fig. 6) and already at this bi-variate stage, it is possible to rank the mean-biserial values from the parameter with the highest explanatory power to the least one. Out of these, we choose here to highlight the most prominent ones: Drs (0.27), Id (0.26), PGD (0.26), and Dsq (0.25). Notably, for certain shaking parameters such as Pa, Ic and Arms, their respective distributions appear very heavy-tailed, making their linear use difficult, if correlated with landslide occurrences.

We further analysed the spatial bivariate correlation using Moran's I and the LISA clustering (see Appendix A). This is geographically shown in Figure 7. There, we can observe that similarly to the information conveyed by the violin plots, the highest spatial correlation is now achieved using the Drs parameter. In such cases, Drs shows a number of True Positives comparable to those estimated for CUD and Iv. However, Moran's I value in Drs

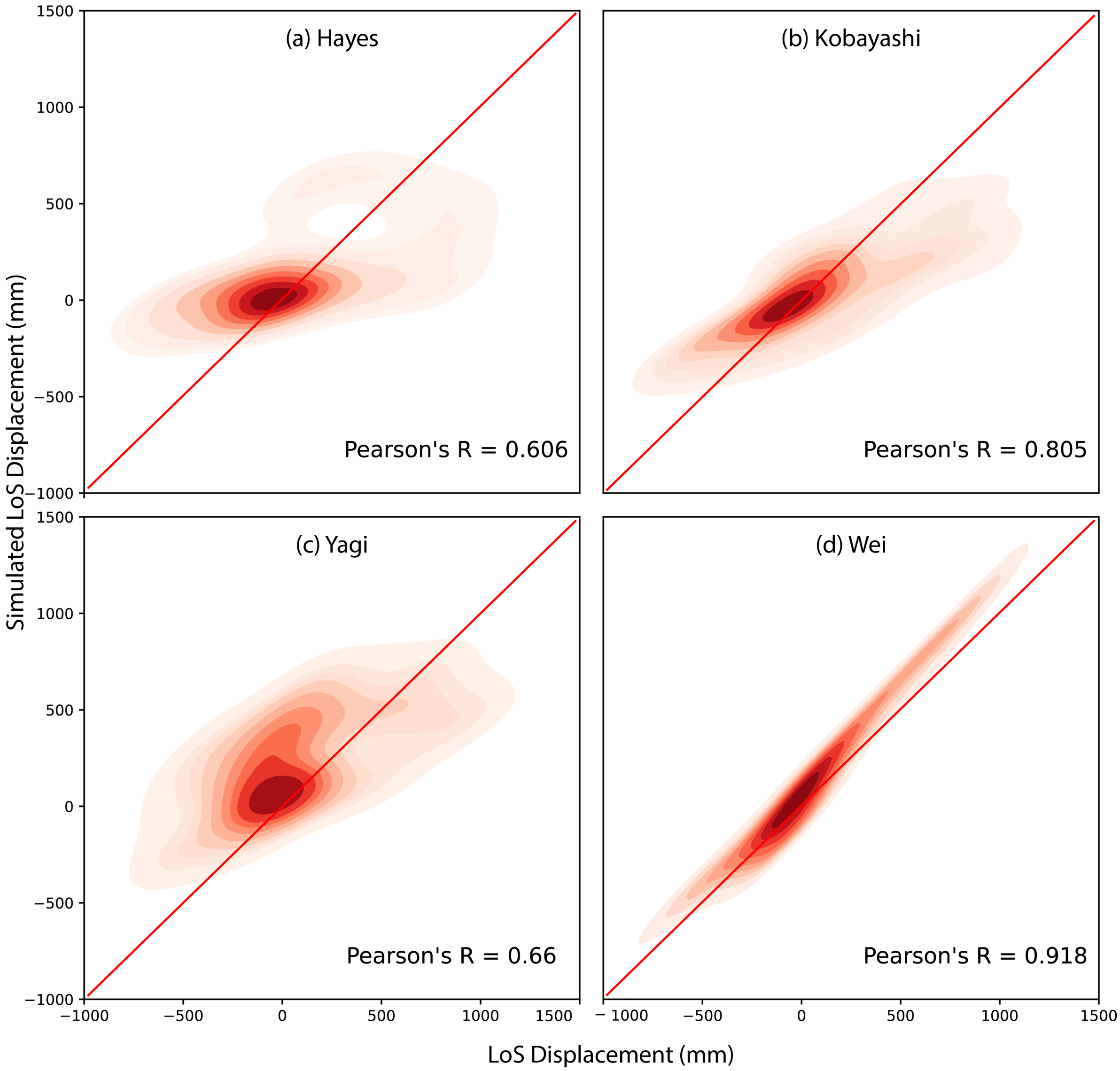

Figure 4: Two-dimensional density plot for the InSAR-based LoS cumulative displacement and the ground motion simulated one.

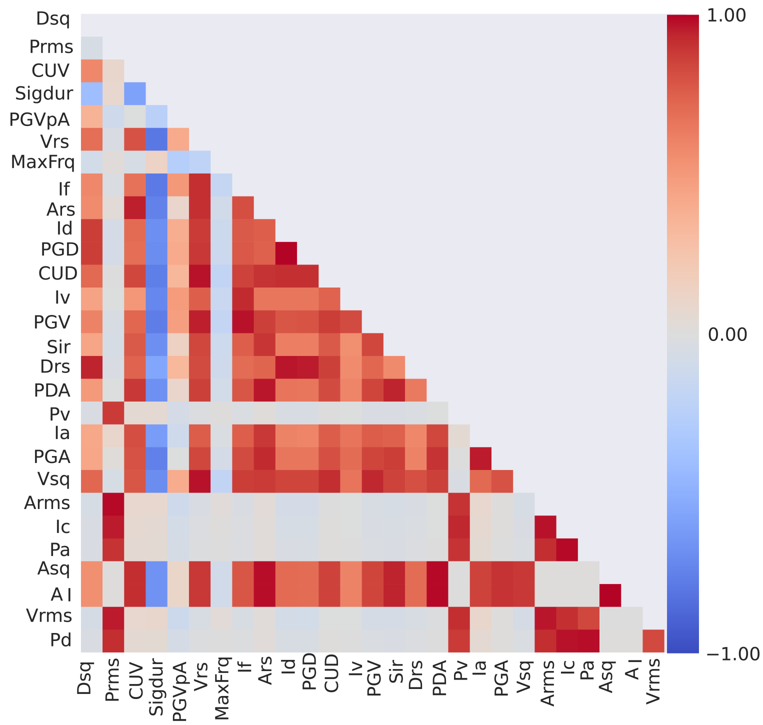

Figure 5: Cross-Correlation between the ground motion parameters extracted from the simulation.

is the highest because it also contains the lowest number of False Positives.

Even if we noticed Drs to be the best bi-variately performing parameter, we cannot state at this stage whether this is valid in a multivariate framework. To answer this question, we featured all intensity summaries as part of a GAM equipped with a variable selection routine. These results are shown in Figure 8.

There, we rank the AIC values for each parameter set, sorted from the best single variable model to the best pair, then to the best triplet and so on. What stands out the most is that after the inclusion of the 10^{th} parameter (PGD), AIC values cease to significantly decrease. Notably, a stepwise variable selection is not really designed to address collinearity issues (Katrutsa and Strijov, 2017). For this reason, despite the selection of ten parameters, some residual collinearity still appeared among them with PGD and Ars being strongly correlated to other properties. For this reason, we also removed these two and built a binomial GAM with the remaining eight.

The partial dependence plots estimated from the fitted model is shown in Figure 9. There, each nonlinear effect on the Gorkha susceptibility model can be compared to one another. For instance, Dsq appears to exert an almost linear contribution to the probability of coseismic landslide occurrence and it is also the covariate with the narrowest confidence interval. However, the largest variations to the susceptibility pattern are brought by CUV, Vrs, Prms and PGVpA. As for the remaining Sigdur, MaxFrq and If, these covariates appear to be almost not significant (most of the width of the 95% confidence interval contains the

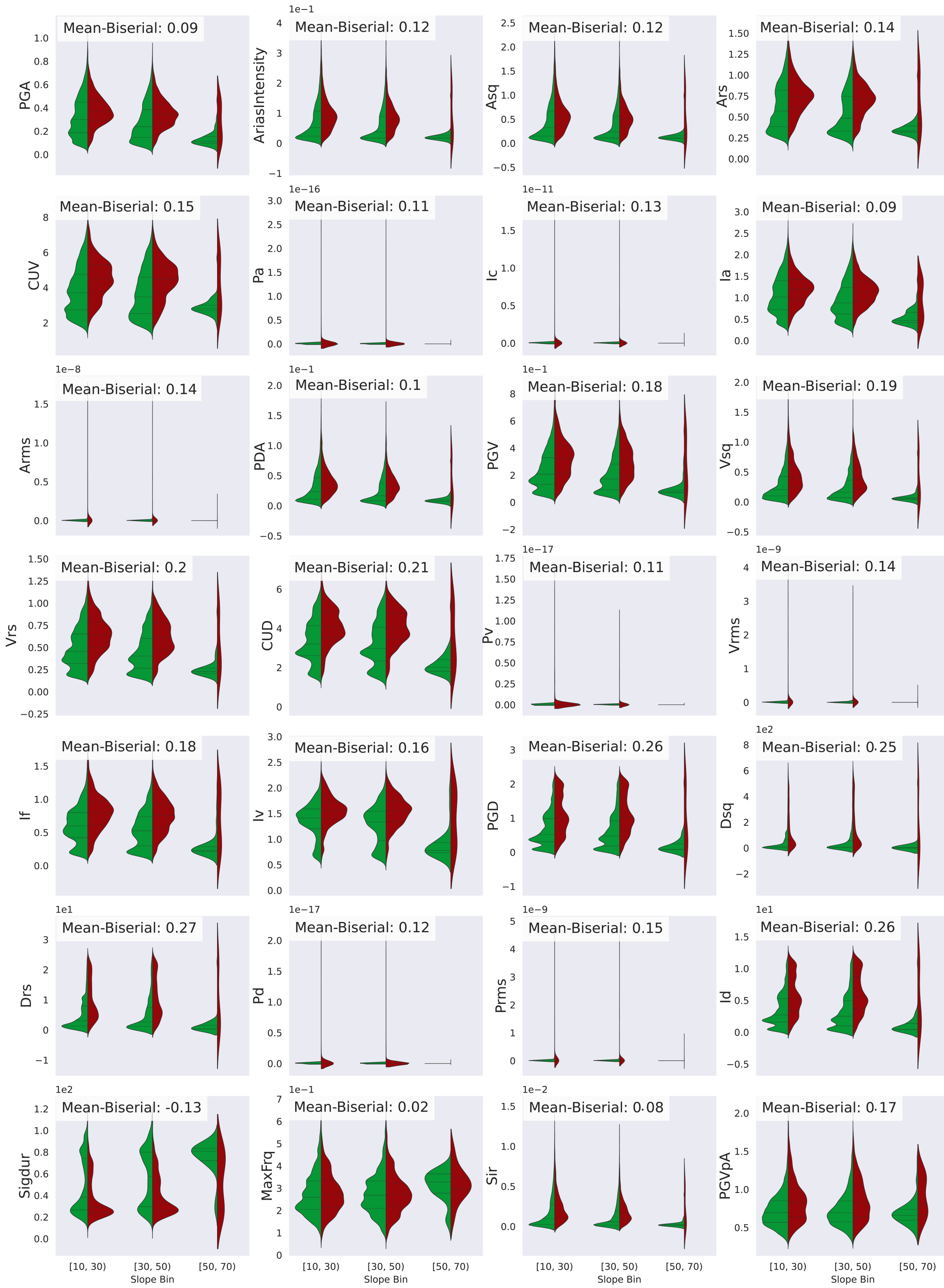

Figure 6: Violin plots representing the distribution of ground motion parameters across multiple slope categories. Their respective average bi-serial correlation is listed at the top left of each sub-panel.

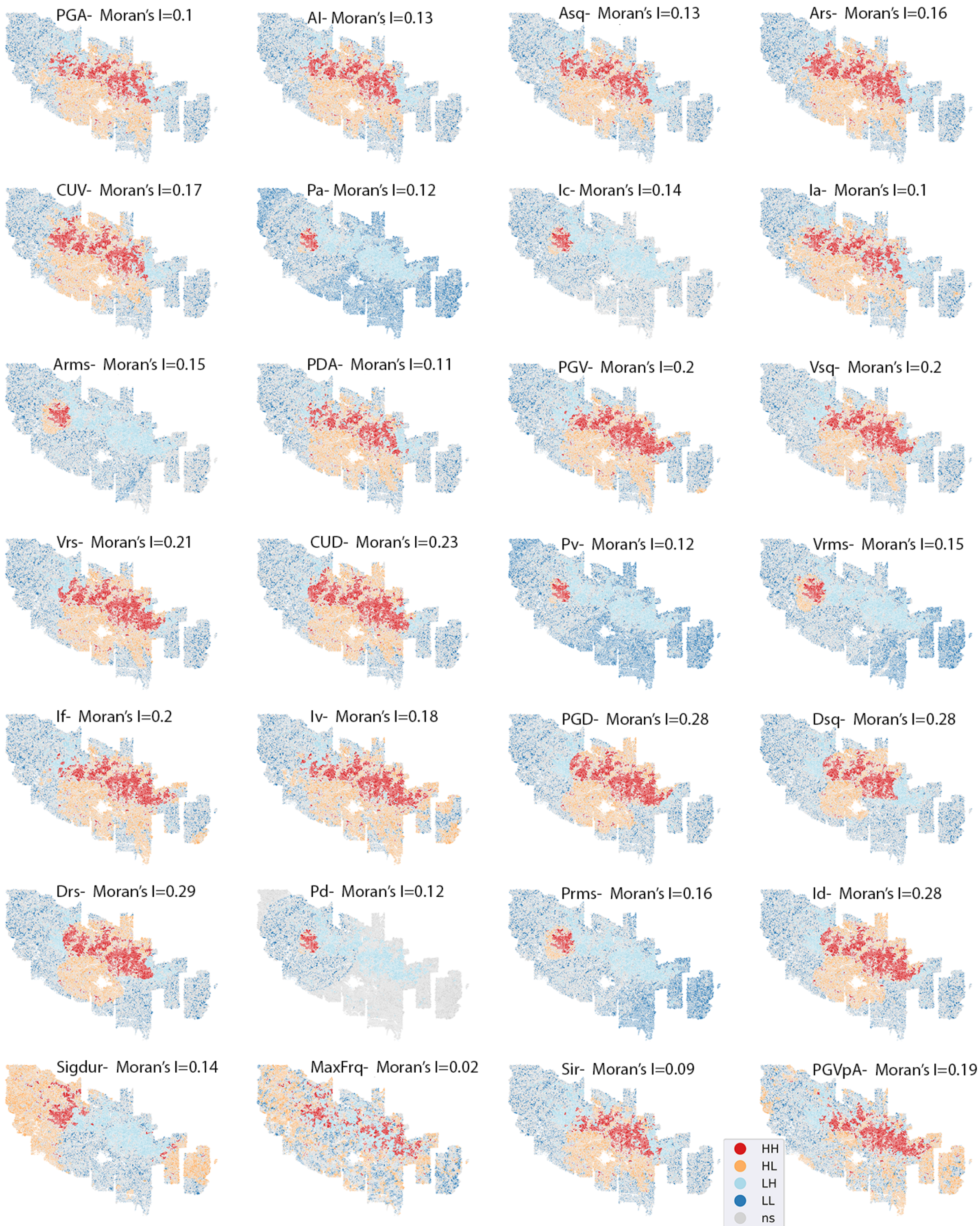

Figure 7: Local Bivariate LISA plot and Moran's I value showing the spatial correlation and clustering of the landslides and the ground motion parameters. HH: High-High clustering, HL: High-Low clustering, LH:Low-High clustering,and LL:Low-Low clustering, where first letter represnts the ground motion parameter and second ltter represents the landslide.

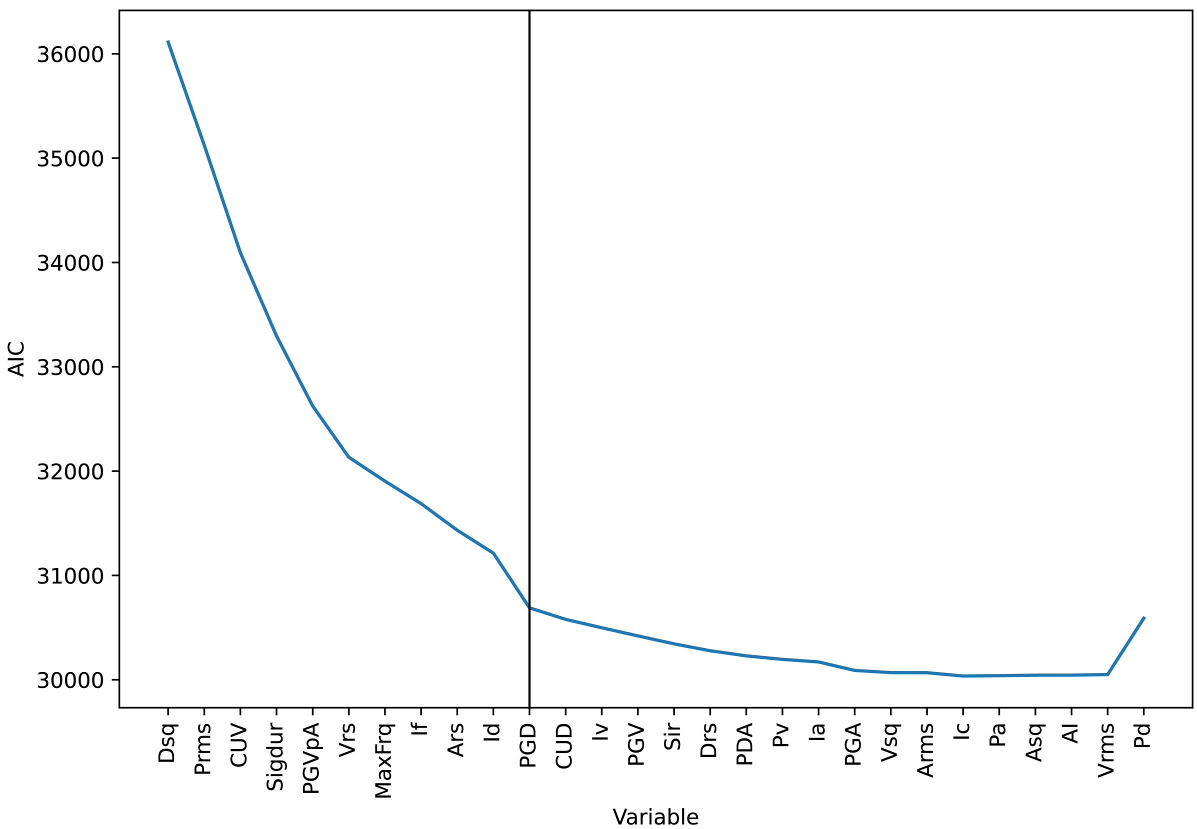

Figure 8: Variation in AIC values with the addition of new variables to the previously selected one.

zero line).

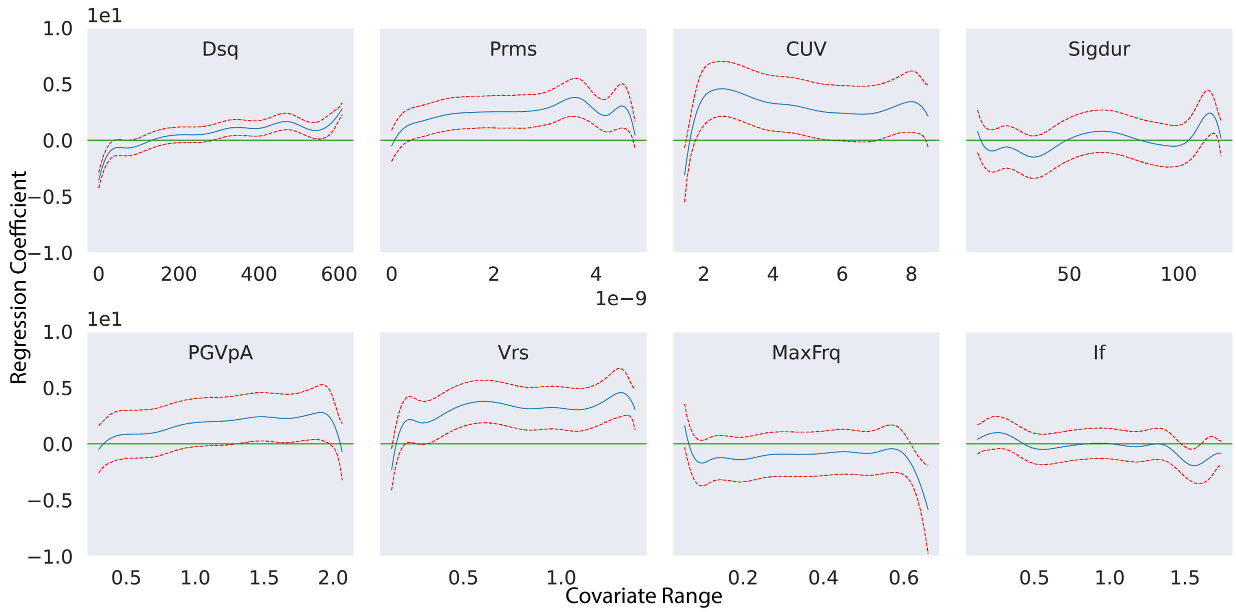

Figure 9: Partial dependence of the ground motion parameters in the fitted binomial GAM. The blue line represents the mean nonlinear effect, the two red lines define the 95% confidence interval and the green one corresponds to the line where the regression coefficient is zero.

Aside from the interpretation aspects, one interesting question is to understand whether a susceptibility model that relies on synthetic ground motion can produce a better spatial prediction as compared to the standard inclusion of GMPEs-based solutions (MMI, PGV, and PSA) from the USGS ShakeMap system (García et al., 2012). To address this question, we performed the same analyses done before by initially examining pairwise correlations among GMPE solutions and then building a binomial GAM with the GMPE-related best set. Figure 10 shows very high interdependence among these shaking parameters; hence we tested them all and selected the PGA as the single best. Notably, the USGS updated all the ground motion parameters for the Gorkha earthquake with time. For this reason, we opted to present the result of susceptibility models built with each PGA update and to compare those to our final model relying on eight synthetic parameters as well as our own PGA alone. These results are shown in Figure 11, where we can observe that the model based on multiple ground motion properties outperforms every other single-variable model. However, the PGA-only model based on the data the USGS released in 2020 performs better than the PGA-only model we obtained using our synthetic data. In Section 6 we will further provide our interpretation of why this is the case. Here we complete the overview by showing the results of the LISA model, highlighting the spatial autocorrelation between the actual landslide distribution and the models obtained with the USGS-PGA and our own with eight covariates (see Fig. 12).

Moran's I appears to be much larger when using synthetic ground motion parameters.

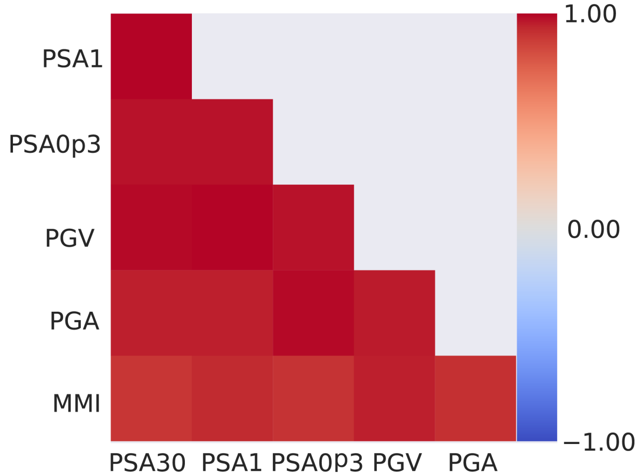

Figure 10: Correlation plot of the USGS provided ground motion data.

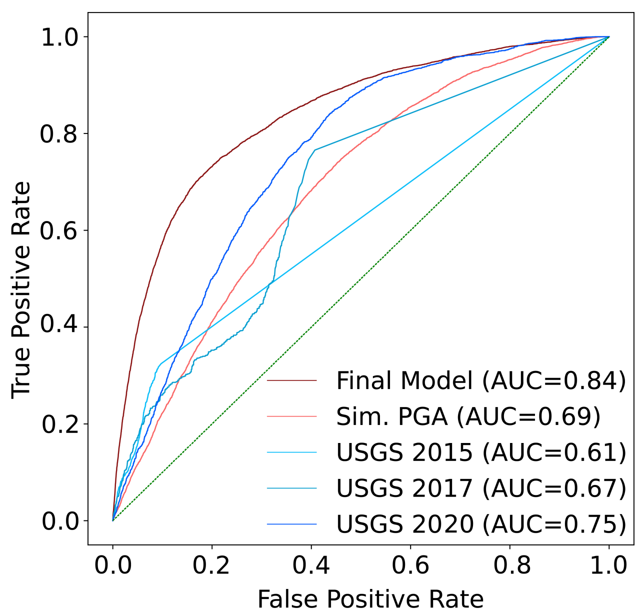

Figure 11: AUC plot with the fitted model and ground motion parameters from USGS. Sim. PGA refers to the model based on our own PGA alone and Final Model corresponds to the one relying on eight synthetic parameters of the simulated PGA.

Even though in Figure 11 the AUC difference between the two models is 0.09, the difference in Moran's I is 0.17. This corresponds to a relative improvement of $\approx 62\%$. Aside from pure numerical considerations, the spatial patterns are also visibly better when using synthetic data. In fact, the number of False Positives drastically decreases in the second panel.

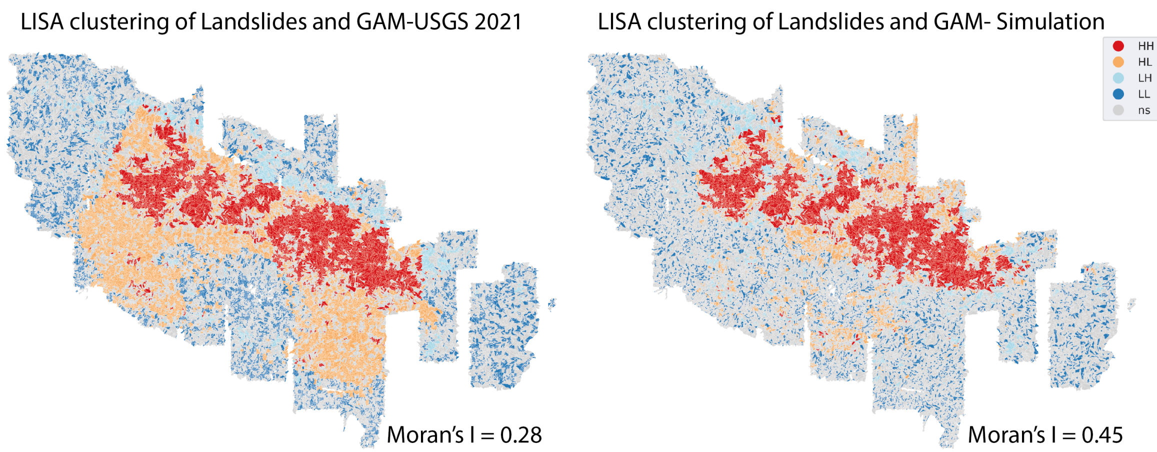

Figure 12: Overview of spatial autocorrelation between the single-variable model that uses the USGS-PGA from 2020 and the Final model that uses our synthetic parameters.

6 Discussion

The following sections will separately elaborate considerations on two different aspects: ground motion simulation and landslide evaluation.

6.1 Ground motion simulation

Based on the four different finite fault models, results show that the best simulation was with the finite fault model from Wei et al. (2018), for it provided better fit both in terms of amplitude and phase timing when examining the recorded ground motion compared data (see Fig. 2). The same model proved to be the best also in terms of InSAR-based considerations (Fig. 4), for it showed a very strong correlation between satellite- and synthetic-based cumulative displacements. It is important to stress here that Wei et al. (2018) used a large number of InSAR data-points in their fault inversion. As a result, the correlation between synthetic and observed displacements is to be expected. Even though this is the case, it should not be considered a weakness but rather a sign that the inversion the authors performed is reliable. Moreover, using InSAR as a validation tool, one must also consider the simulation frequency range as well as the dominant frequency range of the earthquake because displacement caused by large frequency waves cannot be observed from the InSAR data. In any case, our choice is also confirmed with station data. In this case, some additional considerations should be made in relation to the match between simulated and observed ground motion (Fig. 2). Specifically, the NAST and KATNP stations both show significant oscillations along the E-W and N-S directions after the S-wave arrival. This is most likely due to soil amplification within the sedimentary basin of the Kathamandu valley. In fact, the basin structure and resulting soil amplification in the valley are not well represented in any of our simulations because we lack information on the 3D earth velocity structure. The subsurface model we used is very coarse and provides a smoothed representation of the P- and S-wave velocity structure, something that results in a limited spatial variation in all directions other than the vertical one. This being said, our research focuses exclusively on coseismic landsliding. As a result, the mismatch within the Kathmandu basin is of no practical relevance because flat areas are actually removed ($< 10°$ steepness) from the susceptibility analyses (Kritikos et al., 2015).

The major limitation in our simulations has to do with the frequency content. In fact, the four finite fault models have been designed with a respective maximum inversion frequency ranging from 0.25 to 1.0 Hz. As a result, it is also difficult to synthetically radiate high frequencies. Furthermore, the Gorkha earthquake nucleated and propagated along approximately 150 km the fault (MHT). Thus, it affected a large region forcing us to extend our simulation domain in a geographic space of $3° \times 4°$. In such a domain, the mesh creation could not resolve very high frequencies as the computational costs would raise drastically. Nevertheless, even our maximum resolved frequency of 3.0 Hz should be suitable for this specific earthquake for it has been reported in a number of publications that the dominant frequency ranged between 0.25-0.3 Hz in all directions (Parajuli and Kiyono, 2015).

6.2 Geostatistical evaluation of landslides

We envisioned this experiment because coseismic landslides are almost unanimously modelled by using GMPE-based solutions and specifically the PGA accessed at the USGS ShakeMap System. Our hypothesis is that the genesis of landslides may be due to factors that go beyond the mere PGA. For this reason, we generated a suite of synthetic seismic parameters, each one explaining a different aspect of the interaction between wavefields and topographies. Our results (see 6) highlight that parameters such as the Drs is the property with the highest point-biserial correlation with respect to the landslide scenario. We recall here that Drs is calculated as the square root of the cumulative squared displacement. Thus, it represents an absolute value of the total displacement. The common peak ground displacement (PGD) alternative can only inform on maximum values whereas Drs is a summary of the full waveform. Other variables, such as PGD and Dsq also showed high point-biserial correlations, meaning that in general, displacement-related parameters tend to better explain the landslide distribution compared to acceleration and velocity metrics. However, the intensity with which a particle is exposed to may not be the only cause of slope failures. Another reason could be the duration of the shaking itself. This may be the reason why Significant duration (Sigdur) appears to be among the parameters with the largest association to landslides.

Similar considerations arise when looking at the spatial autocorrelation patterns in Figure 7. There, analogous ranks can be seen in the Moran's I values with the best parameters standing out in the bivariate analyses being also the ones that have the largest number of True Positives and the smallest of False Negatives.

Moving to the multivariate analyses, the variable selection opens up considerations on variable interactions. Specifically, the information each seismic parameter carries does not inform on the full waveform signal and its destabilizing effect on slopes. However, a multivariate approach can borrow strength by combining each seismic information. This can be seen in the selection of eight dominant covariates (see Fig. 8).

In addition to the information on the absolute cumulative displacement brought by Dsq (see above), RMS power index (Prms) and Root squared velocity (Vrs) would play a similar role, increasing the probability of coseismic landsliding. Notably, they have both been computed as the root mean square of the significant displacement and total velocity, respectively. Here significant refers to the terminology used by Trifunac and Todorovska (2001), indicating the part of the full waveform that is not zero nor noise. The term total refers instead to the integration of the velocity spectrum over the whole time series. Thus, they inform the model of the intensity and rate at which particles on a soil column are perturbed by the earthquake. As for the Cumulative velocity (CUV), this parameter also acts positively within the model. Differently from Vrs though, this parameter considers also the ground motion phases, thus bringing information on the overall resulting effect of particle velocities hanging on a slope. Furthermore, ratio of PGA and PGV (PGVpA) also contributed to increasing the susceptibility. Being computed as the ratio between PGV and PGA, this means that when the velocity at which particles oscillate is persistently high over time as compared to short-term velocity variations, the slope will be more prone to fail. This is something that intuitively gives value to our experiment for similar considerations have been otherwise impossible in a traditional context. Our interpretation is that a large and prolonged high velocity is justified to exhibit a positive influence as compared to a short-duration one because the latter may not bring the slope to the brink of failure but the latter could definitely perturb its equilibrium for so long that it triggers a landslide. A very similar consideration applies to Sigdur for this covariate precisely conveys the significant duration of the ground motion. In fact, whether a cluster of particles oscillates in one direction or another or with a certain frequency or another, if these phenomena occur with a short or prolonged duration should make a difference, which is what we assume to be captured by Sigdur. Figure 9 shows an overall positive contribution to the final landslide occurrence probability although most of its 95% confidence interval contains the zero line. As a result, Sigdur is the first covariates of the ones discussed so far that exhibits limited statistical significance. The same is also valid for maximum frequency (MaxFrq) and compound index (If), the former still showing an average effect far from the zero regression coefficient mark and the latter being mostly aligned along the same non-contributing level. In turn, this implies that most of the variation in landslide susceptibility is explained by six significant covariates and that the last two may bring some minor details. These can be explained by understanding how they have been computed and what they may indicate. MaxFrq corresponds to the dominant frequency at a particular location obtained by extracting the frequency with the maximum amplitude in the spectral domain. As a result, the slightly negative contribution it shows can be explained with long period oscillations being mostly responsible for landslides occurrences. However, here it is important to stress that our simulations did not contain very high frequencies, to begin with. Therefore the interpretation of this property needs to be re-adjusted to the short range we simulated for, with a maximum of 3.0 Hz. This may also be the reason why this covariate appears mostly not-significant and in another geographic contexts where high frequency simulations are possible, it could theoretically give rise to entirely different results. Ultimately, If essentially corresponds to a combination of PGV and duration. For this reason, its limited and non-significant contribution may be due to CUV and Sigdur largely capturing this effect.

The results from the fitted model when compared with the USGS GMPEs' products show an interesting pattern (see Fig. 11). We can clearly see that the full waveform simulation can provide better modelling results when the eight parameters are multivariately used (AUC of 0.84). However, when focusing on our synthetic PGA against those produced by USGS through the years some differences must be acknowledged. Firstly, we can see that the GMPEs' output in 2015 right after the Gorkha event produced a very low AUC (0.61). However, subsequent versions of the same were more informative, leading to better performance with an AUC of 0.67 for the 2017 product and an AUC of 0.75 for the 2020 one. This is due to USGS constraining more and more the GMPE as they collected more data (Allstadt et al., 2018). For instance, the PGA obtained in 2020 includes terrain characteristics and slope in its empirical formulation. Moreover, the authors implemented an optimisation step to match the ground motion observations, they included VS_{30} information. Ultimately, they also run several GMPE and retrieved the final PGA as a weighted ensemble of all the single outputs. Therefore, the PGA obtained in 2020 represents the fruit of a five-year effort by the USGS, and it also included information that was not accessible to us. For instance, we had no notion of the shallow velocity field (no VS_{30}). The most relevant consideration may be related once more to the frequency limitations we encountered. In fact, GMPEs can be used to empirically estimate large frequency ranges, far beyond the 3.0 Hz we simulated for. And, because PGA is the shaking parameter mostly linked to high frequencies, the recent USGS product may be more suitable than our own PGA alone. However, when examining the LISA plot (Fig. 12), the Moran's I appears quite low (0.28), and the spatial autocorrelation between landslide inventory and PGA produces large patterns of False Positives propagating towards the south of the study area. Conversely, our model built on the basis of the eight ground motion parameters produces excellent Moran's I results (0.45) and very few False Positives and Negatives. The difference may be due to the fact that as elaborate the 2020 GMPE may be, it still produces very smooth PGA values along the footwall mainly as a function of distance from the rupture and attenuation. Conversely, the combination of synthetic parameters limits this overestimation.

7 Conclusion

The use of ground motion simulations to examine coseismic landslides are quite limited in the literature (Harp et al., 2014; Chen and Wang, 2022; Dunham et al., 2022; Feng et al., 2022; Sun and Huang, 2023). Their focus mainly gravitates around better assessment of landslide displacements by coupling their simulation results with physically-based methods or the effect of topographic amplification on landslide sizes. In this context, they mostly target capturing peak ground motion values (e.g., PGA, PGV and/or PGD) in a more accurate way. In this work, we take a very different stance by hypothesising that landslides are the product of the interaction between the terrain and the full waveform rather its single peak. For this reason, we generated a full suite of ground motion parameters to be bivariately and multivariately used to model coseismic landslide susceptibility. Our observations indicate that with a maximum simulation frequency of 3.0 Hz, displacement-related parameters largely explain the landslide distribution, in addition to velocity and duration ones.

Any future development from this angle will also rely on ground motion simulations. However, the choice of the study area will determine the extent to which one can dive into the problem. In fact, the density of seismic stations influences the capacity to resolve the earthquake source characteristics and from there to produce meaningful simulations. Nepal, as most countries, is not equipped with a dense seismic network and this certainly affected our ability to simulate for high frequencies. Future experiments may need to be placed in places such as Japan, where the station density is particularly favourable. Moreover, even if we extended our seismic parameters far beyond the few considered in the literature, our 28 ground motion characteristics are still individual representations of the whole time series. A likely better venue to explore would welcome the use of the whole time series into the susceptibility model rather than being approximated into single summaries. As for the regional landslide model itself, the choice of a susceptibility context is also largely improvable. In fact, whether a slope is unstable may not be the most relevant information. Estimating how large coseismic landslides may in fact complement the pure occurrence location studies.

8 Acknowledgement

We would like to thank Jean-Philippe Avouac for sharing the processed high-rate GPS data used in (Galetzka et al., 2015). The project was supported by King Abdullah University of Science and Technology (KAUST) in Thuwal, Saudi Arabia, Grant URF/1/4338-01-01.

9 Author contributions

The work was carried out by Ashok Dahal with support from co-authors. The experiment was co-designed and drafted in a manuscript together with Luigi Lombardo. Martin Mai, David Alejandro Castro Cruz, Islam Fadel and Mark van der Meijde helped with the parameterization of the ground motion simulations. Raphael Huser helped design a suitable statistical analytical protocol. Hakan Tanyas reviewed and edited the manuscript and redesigned the figures for aesthetic and qualitative betterment. Cees van Westen helped to interpret the model results.

A Overview of statistical tests

The cross correlation between the parameters indicates the (dis)similarity between continuous properties and specifically between two ground motion parameters in this work. Ranging from -1 to $+1$, the former implies a perfect positive correlation where an increase of one parameter also increases the other at the same rate and vice versa. Similarly, the latter example implies that the increase in one parameter causes a decrease in the other at the same rate. The correlation coefficient is here calculated pairwise using a Pandas Library in python (pandas development team, 2020). The actual formulation of the correlation coefficient is given by 1.

Moreover, to understand how landslides and ground motion parameters are correlated in different slope domains, we grouped slope units into three different bins of 10°- 30°, 30°-50° and 50°-90° to obtain point-biserial correlation coefficients. The point-biserial correlation is a similar concept to the correlation coefficient explained above, though it addresses a response variable which is dichotomous in nature. The mathematical formulation to calculate the point-biserial correlation coefficient is given by 2.

$$r_{pb} = \frac{(\overline{y}_1 - \overline{y}_2) \cdot \sqrt{pq}}{s_y}, \tag{2}$$

where, p is the proportion for which the nominal value is 1, q represents the proportion for which the nominal value is 0, $\overline{y}_1$ is the conditional mean of the quantitative or numerical variable y when the nominal score is 1, $\overline{y}_2$ is the conditional mean of the quantitative or numerical variable y when the nominal score is 0, and s_y represents the standard deviation of the numerical property.

The point-biserial correlation can certainly provide information on how strong the relationship is between the ground motion parameters and the landslide occurrence but it fails to provide information on their spatial dependence. To highlight spatial dependence, we calculated the bi-variate local Moran's I (Anselin et al., 2002). To do so, we created a neighbourhood matrix between the slope units using their centroid location, using the Queen contiguity method (Berry and Marble, 1968). We then used the method illustrated by Anselin et al. (2002) to obtain the Moran's Index. This information does quantify spatial dependence, which we then visualized using the Local Indicator of Spatial Association (LISA) (Anselin, 1995).

To further understand how multiple ground motion parameters interact to influence landslide occurrences, we initially developed a routine for variable selection. The latter was generated as part of a Generalized Additive Model (GAM; Hastie, 2017), for we repeatedly calculated the Akaike Information Criterion (AIC; Akaike, 1998) value for individual ground motion parameters. We started by selecting the parameter with the lowest AIC to be considered the best predictor. Then, as part of an iterative procedure covering the whole parameter space, we proceeded to extract the best combination of two, then three and so on, selecting each time the set that would yield the minimum AIC value. The procedure stops once adding new covariate information does not contribute to the AIC decrease. This stepwise selection can provide numerical information on the best parameter set. However, it does not specifically address collinearity issues (i.e., the linear dependence between one or more covariates responsible for inflated error estimates and convergence issues; Harrell et al., 2001; Amato et al., 2019). For this reason, from the best covariate set, we further removed those variables with $-0.85 >$ pairwise correlation < 0.85.

These resulting variables were used as nonlinear effects as part of a binomial GAM whose performace was evaluated using the area under (AUC) the receiver operating characteristic (ROC) curve (Hosmer and Lemeshow, 2000; Rahmati et al., 2019).

B Validation of ground motion simulation

We compare the simulation results with the records at seven stations (see Fig. 13). Figure 13 compares the simulation and the records in the "NS" direction for the station CHLM using the Kristekova method (Kristeková et al., 2006). The method quantifies the agreement in phase and the amplitude of both signals. In the case of the station CHLM, for the "NS" direction the comparison results in a score of 6.28/10 and 6.87/10 for amplitude and phase respectively.

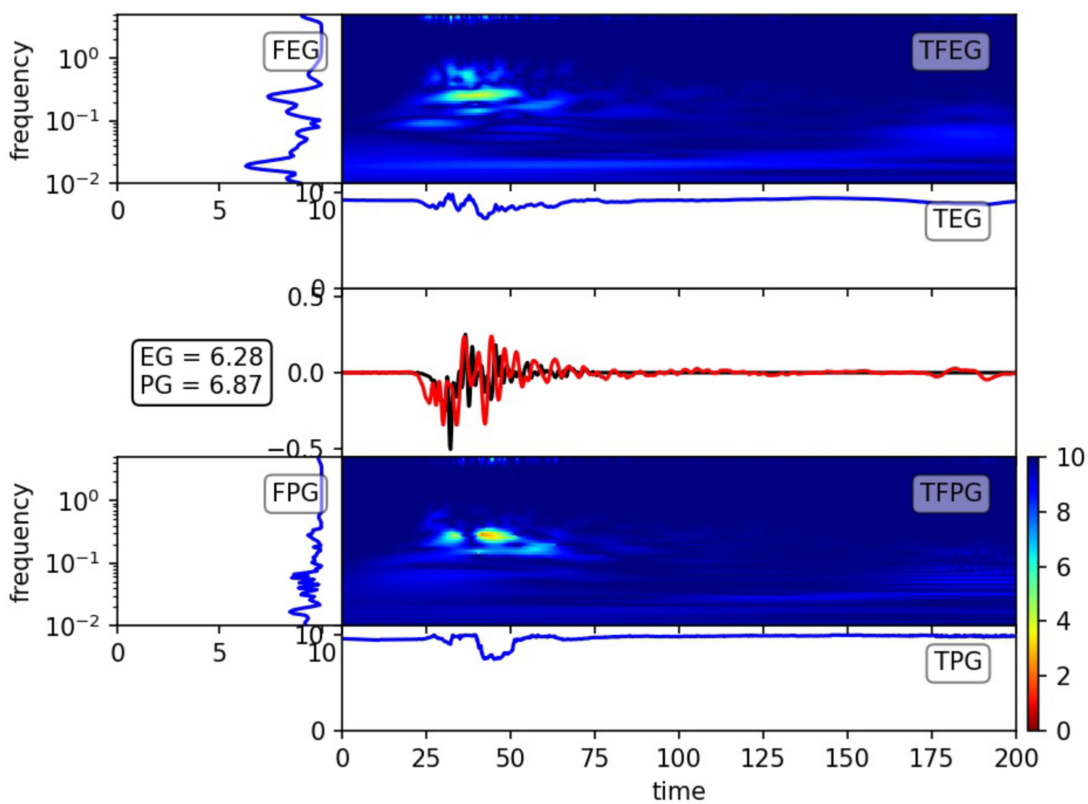

Figure 13: Spectra of the data in acceleration at the station CHLM

The scores for all the other stations, directions, and contemplated faults in this paper are, in most cases, higher than 4 in phase and amplitude (see Fig. 14). For most of them, the score is still upper than 4, meaning that the comparison is fair following the categorization of the method. In general, the source from Wei et al. (2018) and Kobayashi et al. (2016) produce the best fitting among all the alternatives.

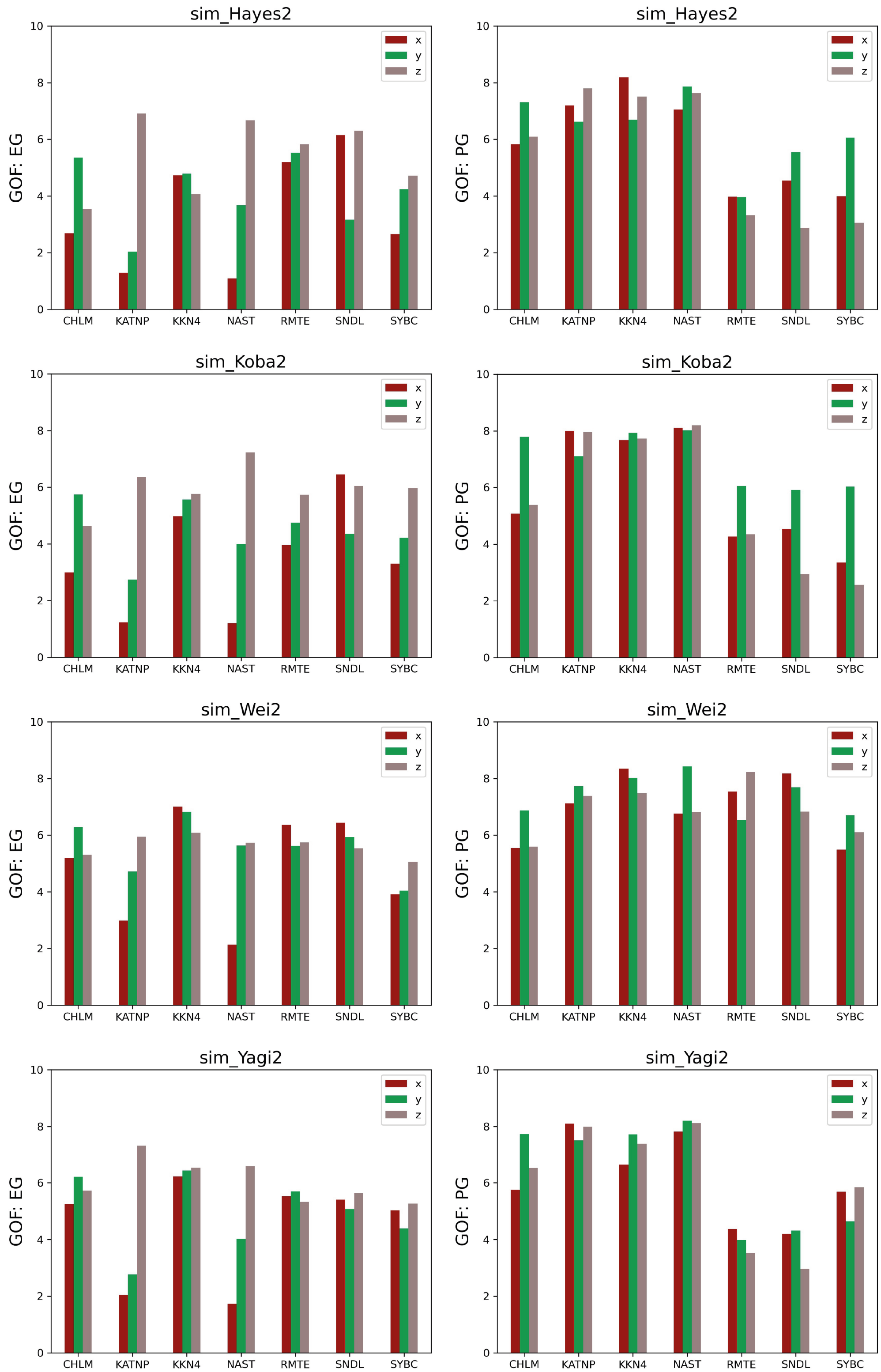

Figure 14: Kristekova values for all cases at all the stations and directions

References

Afanasiev, M., Boehm, C., van Driel, M., Krischer, L., Rietmann, M., May, D. A., Knepley, M. G. and Fichtner, A. (2018) Modular and flexible spectral-element waveform modelling in two and three dimensions. Geophysical Journal International **216**(3), 1675–1692.

Akaike, H. (1998) Information theory and an extension of the maximum likelihood principle. In Selected papers of hirotugu akaike, pp. 199–213. Springer.

Allstadt, K. E., Jibson, R. W., Thompson, E. M., Massey, C. I., Wald, D. J., Godt, J. W. and Rengers, F. K. (2018) Improving Near-Real-Time Coseismic Landslide Models: Lessons Learned from the 2016 Kaikōura, New Zealand, Earthquake. Bulletin of the Seismological Society of America .

Alterman, Z. and Karal Jr, F. (1968) Propagation of elastic waves in layered media by finite difference methods. Bulletin of the Seismological Society of America **58**(1), 367–398.

Alvioli, M., Marchesini, I., Reichenbach, P., Rossi, M., Ardizzone, F., Fiorucci, F. and Guzzetti, F. (2016) Automatic delineation of geomorphological slope units with r.slopeunits v1.0 and their optimization for landslide susceptibility modeling. Geoscientific Model Development **9**(11), 3975–3991.

Amato, G., Eisank, C., Castro-Camilo, D. and Lombardo, L. (2019) Accounting for covariate distributions in slope–unit–based landslide susceptibility models. a case study in the alpine environment. Engineering geology **260**, 105237.

Anselin, L. (1995) Local indicators of spatial association—lisa. Geographical analysis **27**(2), 93–115.

Anselin, L., Syabri, I., Smirnov, O. et al. (2002) Visualizing multivariate spatial correlation with dynamically linked windows. In Proceedings, CSISS Workshop on New Tools for Spatial Data Analysis, Santa Barbara, CA.

Aoi, S., Kunugi, T. and Fujiwara, H. (2004) Strong-motion seismograph network operated by NIED: K-NET and KiK-net. Journal of Japan association for earthquake engineering **4**(3), 65–74.

Araya, R. and Saragoni, R. (1980) Capacidad de los movimientos sísmicos de producir daño estructural.

Arias, A. (1970) A measure of earthquake intensity. seismic design for nuclear power plants. Massachusetts Institute of Technology .

Atkinson, G. M. and Boore, D. M. (2011) Modifications to existing ground-motion prediction equations in light of new data. Bulletin of the Seismological Society of America **101**(3), 1121–1135.

Berry, B. J. and Marble, D. F. (1968) Spatial analysis: a reader in statistical geography. Prentice-Hall.

Bouchon, M. (1985) A simple, complete numerical solution to the problem of diffraction of sh waves by an irregular surface. The Journal of the Acoustical Society of America **77**(1), 1–5.

Castro-Cruz, D., Gatti, F. and Lopez-Caballero, F. (2021) Assessing the impact of regional geology on the ground motion model variability at the kashiwazaki-kariwa nuclear power plant (japan) via physics-based numerical simulation. Soil Dynamics and Earthquake Engineering **150**, 106947.

Chen, C. W. and Zebker, H. A. (2002) Phase unwrapping for large sar interferograms: Statistical segmentation and generalized network models. IEEE Transactions on Geoscience and Remote Sensing **40**(8), 1709–1719.

Chen, Z. and Wang, G. (2022) Sem-newmark sliding mass analysis for regional coseismic landslide hazard evaluation: A case study of the 2016 kumamoto earthquake. In Conference on Performance-based Design in Earthquake. Geotechnical Engineering, pp. 342–352.

Chiou, B., Darragh, R., Gregor, N. and Silva, W. (2008) NGA project strong-motion database. Earthquake Spectra **24**(1), 23–44.

Dahal, A. and Lombardo, L. (2022) Explainable artificial intelligence in geoscience: a glimpse into the future of landslide susceptibility modeling. ESS Open Archive .

Dashti, S., Bray, J. D., Pestana, J. M., Riemer, M., Wilson, D. et al. (2010) Centrifuge testing to evaluate and mitigate liquefaction-induced building settlement mechanisms. Journal of geotechnical and geoenvironmental engineering **136**(7), 918.

Donati, L. and Turrini, M. (2002) An objective method to rank the importance of the factors predisposing to landslides with the GIS methodology: application to an area of the Apennines (Valnerina; Perugia, Italy). Engineering Geology **63**(3-4), 277–289.

Dunham, A. M., Kiser, E., Kargel, J. S., Haritashya, U. K., Watson, C. S., Shugar, D. H., Hughes, A. and DeCelles, P. G. (2022) Topographic control on ground motions and landslides from the 2015 Gorkha earthquake. Geophysical Research Letters p. e2022GL098582.

Ekström, G., Nettles, M. and Dziewoński, A. (2012) The global cmt project 2004–2010: Centroid-moment tensors for 13,017 earthquakes. Physics of the Earth and Planetary Interiors **200-201**, 1–9.

EPRI, A. (1988) criterion for determining exceedance of the operating basis earthquake. rapport np-5930 2848-16. Electric Power Research Institute, USA .

Faccioli, E., Maggio, F., Quarteroni, A. and Taghan, A. (1996) Spectral-domain decomposition methods for the solution of acoustic and elastic wave equations. Geophysics **61**(4), 1160–1174.

Fajfar, P., Vidic, T. and Fischinger, M. (1990) A measure of earthquake motion capacity to damage medium-period structures. Soil Dynamics and Earthquake Engineering **9**(5), 236–242.

Fan, X., Scaringi, G., Korup, O., West, A. J., van Westen, C. J., Tanyas, H., Hovius, N., Hales, T. C., Jibson, R. W., Allstadt, K. E. et al. (2019) Earthquake-induced chains of geologic hazards: Patterns, mechanisms, and impacts. Reviews of geophysics **57**(2), 421–503.

Feng, K., Huang, D., Wang, G., Jin, F. and Chen, Z. (2022) Physics-based large-deformation analysis of coseismic landslides: A multiscale 3d sem-mpm framework with application to the hongshiyan landslide. Engineering Geology **297**, 106487.

Galetzka, J., Melgar, D., Genrich, J. F., Geng, J., Owen, S., Lindsey, E. O., Xu, X., Bock, Y., Avouac, J.-P., Adhikari, L. B. et al. (2015) Slip pulse and resonance of the kathmandu basin during the 2015 gorkha earthquake, nepal. Science **349**(6252), 1091–1095.

Gallen, S. F., Clark, M. K., Godt, J. W., Roback, K. and Niemi, N. A. (2017) Application and evaluation of a rapid response earthquake–triggered landslide model to the 25 April 2015 Mw 7.8 Gorkha earthquake, Nepal. Tectonophysics **714–715**, 173–187. Special Issue on the 25 April 2015 Mw 7.8 Gorkha (Nepal) Earthquake.

García, D., Mah, R., Johnson, K., Hearne, M., Marano, K., Lin, K., Wald, D., Worden, C. and So, E. (2012) ShakeMap Atlas 2.0: an improved suite of recent historical earthquake ShakeMaps for global hazard analyses and loss model calibration. In World Conference on Earthquake Engineering.

Geli, L., Bard, P.-Y. and Jullien, B. (1988) The effect of topography on earthquake ground motion: a review and new results. Bulletin of the Seismological Society of America **78**(1), 42–63.

Guatteri, M., Mai, P. M. and Beroza, G. C. (2004) A pseudo-dynamic approximation to dynamic rupture models for strong ground motion prediction. Bulletin of the Seismological Society of America **94**(6), 2051–2063.

Gupta, S. D. (1960) Point biserial correlation coefficient and its generalization. Psychometrika **25**(4), 393–408.

Gutenberg, B. and Richter, C. F. (1942) Earthquake magnitude, intensity, energy, and acceleration. Bulletin of the Seismological society of America **32**(3), 163–191.

Harp, E. L., Hartzell, S. H., Jibson, R. W., Ramirez-Guzman, L. and Schmitt, R. G. (2014) Relation of landslides triggered by the kiholo bay earthquake to modeled ground motion-relation of landslides triggered by the kiholo bay earthquake to modeled ground motion. Bulletin of the Seismological Society of America **104**(5), 2529–2540.

Harrell, F. E. et al. (2001) Regression modeling strategies: with applications to linear models, logistic regression, and survival analysis. Volume 608. Springer.

Harris, R. A., Barall, M., Andrews, D. J., Duan, B., Ma, S., Dunham, E. M., Gabriel, A.-A., Kaneko, Y., Kase, Y., Aagaard, B. T. et al. (2011) Verifying a computational method for predicting extreme ground motion. Seismological Research Letters **82**(5), 638–644.

Hastie, T. J. (2017) Generalized additive models. In Statistical models in S, pp. 249–307. Routledge.

Hayes, G. P., Briggs, R. W., Barnhart, W. D., Yeck, W. L., McNamara, D. E., Wald, D. J., Nealy, J. L., Benz, H. M., Gold, R. D., Jaiswal, K. S. et al. (2015) Rapid characterization of the 2015 m w 7.8 gorkha, nepal, earthquake sequence and its seismotectonic context. Seismological Research Letters **86**(6), 1557–1567.

He, J., Qi, S., Wang, Y. and Saroglou, C. (2020) Seismic response of the lengzhuguan slope caused by topographic and geological effects. Engineering Geology **265**, 105431.

Hosmer, D. W. and Lemeshow, S. (2000) Applied Logistic Regression. Second edition. New York: Wiley.

Housner, G. (1975) Measures of severity of earthquake ground shaking. In Proceedings of US National Conference on Earthquake Engineering, 1975. 6.

Housner, G. and Jennings, P. C. (1964) Generation of artificial earthquakes. Journal of the Engineering Mechanics Division **90**(1), 113–150.

Housner, G. W. (1952) Spectrum intensities of strong-motion earthquakes. In Proceedings of the Symposium on Earthquake and Blast Effects on Structures. Earthquake Engineering Research Institute.

Housner, G. W. (1970) Strong ground motion. Earthquake engineering **75**, 91.

Huang, D., Wang, G., Du, C., Jin, F., Feng, K. and Chen, Z. (2020) An integrated SEM-Newmark model for physics-based regional coseismic landslide assessment. Soil Dynamics and Earthquake Engineering **132**, 106066.

Igel, H. (2017) Computational seismology: a practical introduction. Oxford University Press.

Imperatori, W. and Mai, P. M. (2013) Broad-band near-field ground motion simulations in 3-dimensional scattering media. Geophysical journal international **192**(2), 725–744.

Jibson, R. W. (1993) Predicting earthquake-induced landslide displacements using newmark's sliding block analysis. Transportation research record **1411**, 9–17.

Jibson, R. W. (2007) Regression models for estimating coseismic landslide displacement. Engineering geology **91**(2-4), 209–218.

Jibson, R. W. (2011) Methods for assessing the stability of slopes during earthquakes–A retrospective. Engineering Geology **122**(1–2), 43–50.

Jibson, R. W., Harp, E. L. and Michael, J. A. (2000) A method for producing digital probabilistic seismic landslide hazard maps. Engineering geology **58**(3-4), 271–289.

Katrutsa, A. and Strijov, V. (2017) Comprehensive study of feature selection methods to solve multicollinearity problem according to evaluation criteria. Expert Systems with Applications **76**, 1–11.

Khalil, C. and Lopez-Caballero, F. (2021) Survival analysis of a liquefiable embankment subjected to sequential earthquakes. Soil Dynamics and Earthquake Engineering **140**, 106436.

Kobayashi, H., Koketsu, K., Miyake, H., Takai, N., Shigefuji, M., Bhattarai, M. and Sapkota, S. N. (2016) Joint inversion of teleseismic, geodetic, and near-field waveform datasets for rupture process of the 2015 gorkha, nepal, earthquake. Earth, Planets and Space **68**(1), 1–8.

Kristeková, M., Kristek, J., Moczo, P. and Day, S. M. (2006) Misfit criteria for quantitative comparison of seismograms. Bulletin of the seismological Society of America **96**(5), 1836–1850.

Kritikos, T., Robinson, T. R. and Davies, T. R. (2015) Regional coseismic landslide hazard assessment without historical landslide inventories: A new approach. Journal of Geophysical Research: Earth Surface **120**(4), 711–729.

Lee, C.-T. (2014) Statistical seismic landslide hazard analysis: An example from Taiwan. Engineering Geology **182**, 201–212.

Lindsey, E. O., Natsuaki, R., Xu, X., Shimada, M., Hashimoto, M., Melgar, D. and Sandwell, D. T. (2015) Line-of-sight displacement from alos-2 interferometry: Mw 7.8 gorkha earthquake and mw 7.3 aftershock. Geophysical Research Letters **42**(16), 6655–6661.

Lombardo, L., Bakka, H., Tanyas, H., van Westen, C., Mai, P. M. and Huser, R. (2018) Geostatistical modeling to capture seismic–shaking patterns from earthquake–induced landslides. arXiv preprint arXiv:1807.08513 .

Lombardo, L. and Tanyas, H. (2021) From scenario–based seismic hazard to scenario–based landslide hazard: fast–forwarding to the future via statistical simulations. Stochastic Environmental Research and Risk Assessment pp. 1–14.

Lysmer, J. and Drake, L. A. (1972) A finite element method for seismology. Methods in computational physics **11**, 181–216.

Mahesh, P., Rai, S., Sivaram, K., Paul, A., Gupta, S., Sarma, R. and Gaur, V. (2013) One-dimensional reference velocity model and precise locations of earthquake hypocenters in the kumaon–garhwal himalaya. Bulletin of the Seismological Society of America **103**(1), 328–339.

Mai, P. M. and Thingbaijam, K. (2014) Srcmod: An online database of finite-fault rupture models. Seismological Research Letters **85**(6), 1348–1357.

Meltzer, A., Rudnick, R., Zeitler, P., Levander, A., Humphreys, G., Karlstrom, K., Ekstrom, E., Carlson, C., Dixon, T., Gurnis, M. et al. (1999) The USArray initiative. Geological Society of America Today **9**, 8–10.

Millen, M. (2019) eng-tools/eqsig: First production release.

Newmark, N. M. (1965) Effects of earthquakes on dams and embankments. Geotechnique **15**(2), 139–160.

Newmark, N. M. and Hall, W. J. (1973) Procedures and criteria for earthquake-resistant design. In Selected Papers By Nathan M. Newmark: Civil Engineering Classics, pp. 829–872.

Nowicki, M. A., Wald, D. J., Hamburger, M. W., Hearne, M. and Thompson, E. M. (2014) Development of a globally applicable model for near real-time prediction of seismically induced landslides. Engineering Geology **173**, 54–65.

Nowicki Jessee, M., Hamburger, M., Allstadt, K., Wald, D., Robeson, S., Tanyas, H., Hearne, M. and Thompson, E. (2018) A Global Empirical Model for Near–Real–Time Assessment of Seismically Induced Landslides. Journal of Geophysical Research: Earth Surface **123**(8), 1835–1859.

Nowicki Jessee, M. A., Hamburger, M., Ferrara, M., McLean, A. and FitzGerald, C. (2020) A global dataset and model of earthquake-induced landslide fatalities. Landslides **17**(6), 1363–1376.

Oglesby, D. D. and Mai, P. M. (2012) Fault geometry, rupture dynamics and ground motion from potential earthquakes on the North Anatolian Fault under the Sea of Marmara. Geophysical Journal International **188**(3), 1071–1087.

Ord, J. K. and Getis, A. (1995) Local spatial autocorrelation statistics: distributional issues and an application. Geographical analysis **27**(4), 286–306.

Oven, K., Rana, S., Basyal, G. K. and Rosser, N. (2021) Policies, Politics, and practices of Landslide Risk Management in Post-earthquake Nepal. Epicentre to Aftermath: Rebuilding and Remembering in the Wake of Nepal's Earthquakes p. 151.

Pacor, F., Paolucci, R., Luzi, L., Sabetta, F., Spinelli, A., Gorini, A., Nicoletti, M., Marcucci, S., Filippi, L. and Dolce, M. (2011) Overview of the Italian strong motion database ITACA 1.0. Bulletin of Earthquake Engineering **9**(6), 1723–1739.

Paolucci, R., Mazzieri, I. and Smerzini, C. (2015) Anatomy of strong ground motion: near-source records and three-dimensional physics-based numerical simulations of the m w 6.0 2012 may 29 po plain earthquake, italy. Geophysical Supplements to the Monthly Notices of the Royal Astronomical Society **203**(3), 2001–2020.

Parajuli, R. R. and Kiyono, J. (2015) Ground motion characteristics of the 2015 gorkha earthquake, survey of damage to stone masonry structures and structural field tests. Frontiers in Built Environment **1**, 23.

Park, Y.-J., Ang, A. H.-S. and Wen, Y. K. (1985) Seismic damage analysis of reinforced concrete buildings. Journal of Structural Engineering **111**(4), 740–757.

Pearce, A. J. and Watson, A. J. (1986) Effects of earthquake-induced landslides on sediment budget and transport over a 50-yr period. Geology **14**(1), 52–55.

Pearson, K. (1895) Vii. note on regression and inheritance in the case of two parents. proceedings of the royal society of London **58**(347-352), 240–242.

Peter, D., Komatitsch, D., Luo, Y., Martin, R., Le Goff, N., Casarotti, E., Le Loher, P., Magnoni, F., Liu, Q., Blitz, C. et al. (2011) Forward and adjoint simulations of seismic wave propagation on fully unstructured hexahedral meshes. Geophysical Journal International **186**(2), 721–739.

Poreddy, L. R., Pathapadu, M. K., Navyatha, C., Vemuri, J. and Chenna, R. (2022) Correlation analysis between ground motion parameters and seismic damage of buildings for near-field ground motions. Natural Hazards Research **2**(3), 202–209.

Rahmati, O., Kornejady, A., Samadi, M., Deo, R. C., Conoscenti, C., Lombardo, L., Dayal, K., Taghizadeh-Mehrjardi, R., Pourghasemi, H. R., Kumar, S. et al. (2019) PMT: New analytical framework for automated evaluation of geo–environmental modelling approaches. Science of the total environment **664**, 296–311.

Riddell, R. (2007) On ground motion intensity indices. Earthquake spectra **23**(1), 147–173.

Riddell, R. and Garcia, J. E. (2001) Hysteretic energy spectrum and damage control. Earthquake engineering & structural dynamics **30**(12), 1791–1816.

Roback, K., Clark, M. K., West, A. J., Zekkos, D., Li, G., Gallen, S. F., Chamlagain, D. and Godt, J. W. (2018) The size, distribution, and mobility of landslides caused by the 2015 Mw7.8 Gorkha earthquake, Nepal. Geomorphology **301**, 121–138.

Robinson, T. R., Rosser, N. J., Densmore, A. L., Williams, J. G., Kincey, M. E., Benjamin, J. and Bell, H. J. A. (2017) Rapid post–earthquake modelling of coseismic landslide intensity and distribution for emergency response decision support. Natural Hazards and Earth System Sciences **17**(9), 1521–1540.

Rosenblueth, E. (1964) Probabilistic design to resist earthquakes. Journal of the Engineering Mechanics Division **90**(5), 189–220.

Ryan, W. B., Carbotte, S. M., Coplan, J. O., O'Hara, S., Melkonian, A., Arko, R., Weissel, R. A., Ferrini, V., Goodwillie, A., Nitsche, F. et al. (2009) Global multi-resolution topography synthesis. Geochemistry, Geophysics, Geosystems **10**(3).

Sandwell, D., Mellors, R., Tong, X., Wei, M. and Wessel, P. (2011) Open radar interferometry software for mapping surface deformation.

Schmitt, R. G., Tanyas, H., Jessee, M. A. N., Zhu, J., Biegel, K. M., Allstadt, K. E., Jibson, R. W., Thompson, E. M., van Westen, C. J., Sato, H. P., Wald, D. J., Godt, J. W., Gorum, T., Xu, C., Rathje, E. M. and Knudsen, K. L. (2017) An open repository of earthquake–triggered ground–failure inventories. U.S. Geological Survey Data Series 1064 .

Seriani, G. and Priolo, E. (1994) Spectral element method for acoustic wave simulation in heterogeneous media. Finite elements in analysis and design **16**(3-4), 337–348.

Shahaki, K. M. and Celikag, M. (2019) Correlation of ground motion intensity measures and seismic damage indices of masonry-infilled steel frames. Arabian Journal for Science and Engineering **44**(5), 5131–5150.

Shen, W., Yang, D., Xu, X., Yang, S. and Liu, S. (2022) 3d simulation of ground motion for the 2015 mw 7.8 gorkha earthquake, nepal, based on the spectral element method. Natural Hazards pp. 1–19.

Shigefuji, M., Takai, N., Bijukchhen, S., Ichiyanagi, M., Rajaure, S., Dhital, M. R., Paudel, L. P. and Sasatani, T. (2022) Strong ground motion data of the 2015 gorkha nepal earthquake sequence in the kathmandu valley. Scientific Data **9**(1), 1–8.

Simonett, D. S. (1967) Landslide distribution and earthquakes in the bavani and torricelli mountains, new guinea. Landform Studies from Australia and New Guinea pp. 64–84.

Sun, P. and Huang, D. (2023) Regional-scale assessment of earthquake-induced slope displacement considering uncertainties in subsurface soils and hydrogeological condition. Soil Dynamics and Earthquake Engineering **164**, 107593.

Tanyaş, H. and Lombardo, L. (2020) Completeness Index for Earthquake–Induced Landslide Inventories. Engineering geology **264**, 105331.

Tanyaş, H., Rossi, M., Alvioli, M., van Westen, C. J. and Marchesini, I. (2019) A global slope unit-based method for the near real-time prediction of earthquake-induced landslides. Geomorphology **327**, 126–146.

pandas development team, T. (2020) pandas-dev/pandas: Pandas.

Thrastarson, S., van Driel, M., Krischer, L., Boehm, C., Afanasiev, M., Van Herwaarden, D.-P. and Fichtner, A. (2020) Accelerating numerical wave propagation by wavefield adapted meshes. part ii: full-waveform inversion. Geophysical Journal International **221**(3), 1591–1604.

Trifunac, M. and Todorovska, M. (2001) Evolution of accelerographs, data processing, strong motion arrays and amplitude and spatial resolution in recording strong earthquake motion. Soil Dynamics and Earthquake Engineering **21**(6), 537–555.

Trifunac, M. D. and Brady, A. G. (1975) A study on the duration of strong earthquake ground motion. Bulletin of the Seismological Society of America **65**(3), 581–626.

Tripe, R., Kontoe, S. and Wong, T. (2013) Slope topography effects on ground motion in the presence of deep soil layers. Soil Dynamics and Earthquake Engineering **50**, 72–84.

USGS (2015) M 7.8 - 67 km nne of bharatpur, nepal.

Vyas, J. C., Mai, P. M. and Galis, M. (2016) Distance and azimuthal dependence of ground-motion variability for unilateral strike-slip ruptures. Bulletin of the Seismological Society of America **106**(4), 1584–1599.

Wald, D. J., Lin, K.-W. and Quitoriano, V. (2008) Quantifying and qualifying USGS ShakeMap uncertainty. US Geological Survey Reston, VA.

Wald, D. J., Quitoriano, V., Heaton, T. H., Kanamori, H., Scrivner, C. W. and Worden, C. B. (1999) TriNet "ShakeMaps": Rapid generation of peak ground motion and intensity maps for earthquakes in southern California. Earthquake Spectra **15**(3), 537–555.

Wald, D. J., Worden, C. B., Thompson, E. M. and Hearne, M. (2022) Shakemap operations, policies, and procedures. Earthquake Spectra **38**(1), 756–777.

Walsh, J. and Watterson, J. (1987) Distributions of cumulative displacement and seismic slip on a single normal fault surface. Journal of Structural Geology **9**(8), 1039–1046.

Wei, S., Chen, M., Wang, X., Graves, R., Lindsey, E., Wang, T., Karakaş, Ç. and Helmberger, D. (2018) The 2015 gorkha (nepal) earthquake sequence: I. source modeling and deterministic 3d ground shaking. Tectonophysics **722**, 447–461.

Williams, J. G., Rosser, N. J., Kincey, M. E., Benjamin, J., Oven, K. J., Densmore, A. L., Milledge, D. G., Robinson, T. R., Jordan, C. A. and Dijkstra, T. A. (2018) Satellite-based emergency mapping using optical imagery: experience and reflections from the 2015 nepal earthquakes. Natural hazards and earth system sciences **18**(1), 185–205.

Worden, C. and Wald, D. J. (2016) ShakeMap manual online: Technical manual, user's guide, and software guide. US Geol. Surv. pp. 1–156.

Yagi, Y. and Okuwaki, R. (2015) Integrated seismic source model of the 2015 gorkha, nepal, earthquake. Geophysical Research Letters **42**(15), 6229–6235.

Zhang, L., Li, J., Liao, W. and Wang, Q. (2016) Source rupture process of the 2015 gorkha, nepal mw7.9 earthquake and its tectonic implications. Geodesy and Geodynamics **7**(2), 124–131.